Understanding the Nature of an Unusual Post-starburst Quasar with Exceptionally Strong Ne V Emission

Cameren Swiggum[1] , Christy Tremonti[1] , Serena Perrotta[2] , Adam Schaefer[1,3], Ryan C. Hickox[4] , Alison L. Coil[2] ,
Paul H. Sell[5] , Aleksandar M. Diamond-Stanic[6], Jalyn Krause[1], and Gregory Mosby[7]

[1] Department of Astronomy, University of Wisconsin-Madison, Madison, WI 53706, USA; cameren.swiggum@univie.ac.at
[2] Center for Astrophysics and Space Sciences, University of California San Diego, La Jolla, CA 92093, USA
[3] Max Planck Institute for Astrophysics Karl-Schwarzschild-Strasse 1, D-85748 Garching, Germany
[4] Department of Physics and Astronomy, Dartmouth College, Hanover, NH 03755, USA
[5] Department of Astronomy, University of Florida, Gainesville, FL, 32611 USA
[6] Department of Physics and Astronomy, Bates College, Lewiston, ME, 04240, USA
[7] NASA Goddard Space Flight Center, Mail Code: 665, Greenbelt, MD 20771, USA

Abstract

We present a $z = 0.94$ quasar, SDSS J004846.45-004611.9, discovered in the Sloan Digital Sky Survey III (SDSS-III) BOSS survey. A visual analysis of this spectrum reveals highly broadened and blueshifted narrow emission lines, in particular, [Ne V] $\lambda3426$ and [O III] $\lambda5007$, with outflow velocities of 4000 km s^{-1}, along with unusually large [Ne V] $\lambda3426$/[Ne III] $\lambda3869$ ratios. The gas shows higher ionization at higher outflow velocities, indicating a connection between the powerful outflow and the unusual strength of the high ionization lines. The spectral energy distribution and the $i - W3$ color of the source reveal that it is likely a *core* extremely red quasar (ERQ); a candidate population of young active galactic nuclei (AGN) that are violently *blowing out* gas and dust from their centers. The dominance of host galaxy light in its spectrum and its fortuitous position in the SDSS S82 region allows us to measure its star formation history and investigate variability for the first time in an ERQ. Our analysis indicates that SDSS J004846.45-004611.9 underwent a short-lived starburst phase 400 Myr ago and was subsequently quenched, possibly indicating a time lag between star formation quenching and the onset of AGN activity. We also find that the strong extinction can be uniquely attributed to the AGN and does not persist in the host galaxy, contradicting a scenario where the source has recently transitioned from being a dusty submillimeter galaxy. In our relatively shallow photometric data, the source does not appear to be variable at 0.24–2.4 μm in the rest frame, most likely due to the dominant contribution of host galaxy starlight at these wavelengths.

1. Introduction

Quasars are galaxies host to active galactic nuclei (AGN): central regions of galaxies where rapid accretion of matter onto a supermassive black hole (SMBH) occurs. These AGN drive some of the most powerful outflows of gas and dust observed in the universe. An outstanding problem in galaxy formation and evolution concerns the relationship between these AGN-driven outflows and the resultant effects on their host galaxies. Observational studies have revealed quasar outflows as a potential source of star formation regulation and/or quenching, as feedback from AGN may violently disrupt the surrounding interstellar medium (ISM) of their host galaxies (e.g., Blandford & Begelman 2004; Scannapieco & Oh 2004; Vernaleo & Reynolds 2006; Fabian 2012; Kormendy & Ho 2013).

Theoretical models of galaxy evolution indicate that quasar feedback may result from major merger events that trigger rapid gas inflows (e.g., Hopkins et al. 2005, 2006, 2008; Blecha et al. 2018). These events lead to a burst in star formation along with rapid accretion onto the central SMBH. The dramatic disruption of dust and gas due to these mergers causes galaxies at this stage of evolution to appear observationally as submillimeter galaxies or ultra-luminous infrared galaxies (e.g., Sanders et al. 1988; Veilleux et al. 2009; Simpson et al. 2014). Subsequently, energy and momentum from the accreting SMBH couples to the surrounding ISM, causing a galactic-scale *blowout* of gas and dust, thus revealing a visibly luminous quasar (e.g., Sanders et al. 1988; Di Matteo et al. 2005; Rupke & Veilleux 2011; Liu et al. 2013; Rupke & Veilleux 2013; Hopkins et al. 2016).

Observing populations of dust-reddened quasars (Urrutia et al. 2008; Banerji et al. 2012; Glikman et al. 2012) in the process of blowing out gas and dust from their central SMBHs can offer insight into the immediate effects AGN have on their host galaxies. Observationally, this task is difficult as the blowout phase is estimated to be relatively brief on the timescale of galaxy evolution. Wide field spectroscopic surveys such as the Sloan Digital Sky Survey III (SDSS-III; Eisenstein et al. 2011) Baryon Oscillation Spectroscopic Survey (BOSS; Dawson et al. 2013), and their vast data sets yield the ability to compile statistical samples of galaxies at many evolutionary stages. Recently, a population of extremely red quasars (ERQs; Ross et al. 2015; Hamann et al. 2017) with a redshift peak around $z \sim 1$ and a second peak at $z \sim 2$–3 were discovered in SDSS Data Release 12 (DR12). These quasars are selected by their rest-frame UV to mid-IR (MIR) colors from SDSS and the Wide-field Infrared Survey Explorer (WISE; Wright et al. 2010; Lang et al. 2016) as $i - W3 > 4.6$ (AB). BOSS spectra

reveal they are host to a suite of peculiar emission features in the rest-frame UV, of which most notable is the broad, blueshifted, and wingless emission of C IV λ1549. Hamann et al. (2017) imposes an additional selection of the rest equivalent width (REW) of C IV > 100 Å to define a subsample of *core ERQs* that have a more homogeneous suite of emission line properties and represent the strongest candidates for AGN in the blowout phase. The distinctive spectral features of core ERQs insure that they are not simply Type 1 quasars viewed behind an unusually large dust-reddening screen. Additionally, their overall spectral shape from UV to far-IR (FIR) wavelengths is intrinsically different from Type 1 and Type 2 quasars, as well as from a Type 1 quasars behind a dust-reddening screen (see Hamann et al. 2017, Figure 16).

Extremely broad and blueshifted [O III] λλ4959, 5007 has been observed in the near-infrared (NIR) spectra of 24 core ERQs by Perrotta et al. (2019). [O III] is found to be a suitable tracer for *galactic-scale* outflows as the line is a forbidden transition that cannot be produced in the high density, sub-parsec scales of the broad-line region (BLR) near the central AGN. Instead, it is abundant at the low-density kiloparsec scales of the narrow-line region (NLR). The kinematics of the [O III] line have been used to study galactic-scale outflows in Type 2 AGN over a wide range in luminosity and redshift (e.g., Mullaney et al. 2013; Harrison et al. 2014; Zakamska & Greene 2014; Carniani et al. 2015, 2016). The core ERQs of Perrotta et al. (2019) have [O III] widths (w_{90}) in the range of 2053–7227 km s^{-1}. For comparison, a sample of typical blue quasars from Shen (2016) with bolometric luminosities in the range of ERQs (10^{46}–10^{48} erg s^{-1}) have a w_{90} range of ~1000–2000 km s^{-1} (see Perrotta et al. 2019, Figure 6).

Additionally, Perrotta et al. (2019) found the core ERQs to exhibit a strong correlation between [O III] outflow strength and $i - W3$ color, suggesting that the dust surrounding the AGN may assist in the coupling of energy and momentum between the AGN and the ISM. This relationship has been found in other Type 1 and 2 quasar samples as well (DiPompeo et al. 2018). This process may stem from optical and UV radiation emitted by the central AGN being absorbed by the surrounding dust and reemitted at IR wavelengths. In the case that the dusty envelope has a high IR optical depth ($\tau_{IR} > 1$) and sufficiently encompasses the central AGN, the IR photons will repeatedly scatter, building up momentum, which transfers into the surrounding ISM. Analytical calculations (e.g., Murray et al. 2005; Ishibashi & Fabian 2015; Thompson et al. 2015; Ishibashi & Fabian 2016), and radiative transfer calculations (e.g., Proga & Kallman 2004; Krumholz & Thompson 2012, 2013; Bieri et al. 2017) have noted that this coupling mechanism can accelerate AGN winds.

Here we report on SDSS J004846.45-004611.9 (hereafter J0048-0046), a $z \sim 1$ quasar with a dominant host galaxy continuum in addition to broad, blueshifted high ionization emission lines of which most notable is the forbidden [Ne V] λ3426 line. Its spectrum was identified serendipitously via visual inspection of a subset of spectra from BOSS. Upon calculation of its optical-to-IR color, we find that it meets the ERQ selection criterion of $i - W3 > 4.6$. The goal of our study is to determine if J0048-0046 is a candidate *young* AGN driving powerful outflows and whether its novel observational properties such as its spectroscopically dominant host galaxy

and its available time-series photometry can yield new insight into the physical mechanisms of these sources.

This paper is organized as follows: In Section 2, we lay out the multitude of spectroscopic and photometric data sets used to investigate the multiwavelength and time-domain properties of J0048-0046. In Section 3, we analyze the multiwavelength spectral properties of J0048-046 and report on its emission line profiles. In Section 4, we analyze the morphology and stellar continuum to infer its star formation history. In Section 5, we probe optical and IR variability of J0048-0046 at day-to-month-long timescales. We interpret our results in Section 6 and make comparisons to other studies of ERQs and quasars in general. We conclude with a summary of the work in Section 7. Throughout our analysis, we adopt a Λ cold dark matter cosmology of $\Omega_M = 0.315$, $\Omega_\Lambda = 0.685$, and $H_0 = 67.4$ km s^{-1} Mpc^{-1} from the Planck Collaboration et al. (2020). All derived stellar masses and star formation rates (SFRs) assume a Salpeter (1955) initial mass function (IMF).

2. Data

Quasars exhibit a multitude of spectral properties over a wide range of wavelengths. To gain a better understanding of the physical processes at work in J0048-0046, we assemble data from a variety of ground and space-based telescopes tracing the spectral regime from far-UV (FUV) to radio wavelengths.

2.1. Optical and NIR Spectra

2.1.1. SDSS-III/BOSS

J0048-0046 was selected for spectroscopic follow-up in SDSS-III (Eisenstein et al. 2011) as part of the "Reddened Quasars" ancillary program[8], which attempted to target quasars with $E(B - V) > 0.5$ in the Stripe 82 area using a combination of SDSS, Two Micron All Sky Survey (2MASS), and Faint Images of the Radio Sky at Twenty Centimeters (FIRST) photometry. SDSS-III uses the optical 2.5 m wide-angle telescope at the Apache Point Observatory (Gunn et al. 2006). The BOSS spectrograph (Smee et al. 2013) uses fiber-based spectroscopy with 2″ diameter optical fibers. Light that traverses through the fiber is beam split into a blue channel and a red channel with corresponding wavelength ranges of 3600–6350 Å and 5650–10,000 Å. The spectral resolution is in the range of $R = 1560$ at 3700 Å and $R = 2650$ at 6000 Å. Reduction procedures are carried out by the BOSS data reduction pipeline *idlspec2d* described in Dawson et al. (2013).

The BOSS spectrum for J0048-0046 was taken on 2010 January 5, and is a combination of eight individual exposures, each with a 15 minute integration time. The reported SDSS pipeline redshift is $z = 6.937$; however, the spectral fit mistook a broad [O III] 5007 Å line for Lyα. We instead use the reported redshift value z_noqso $= 0.9379 \pm 0.0001$, which omits QSO templates when determining the best-fit spectral template. The SDSS spectrum (see Figure 1) covers 2500–5050 Å in the quasar's rest frame.

2.1.2. SALT/RSS

In order to more accurately constrain the kinematics of the [Ne V] λ3426 line, we obtained follow-up spectrum with a

---
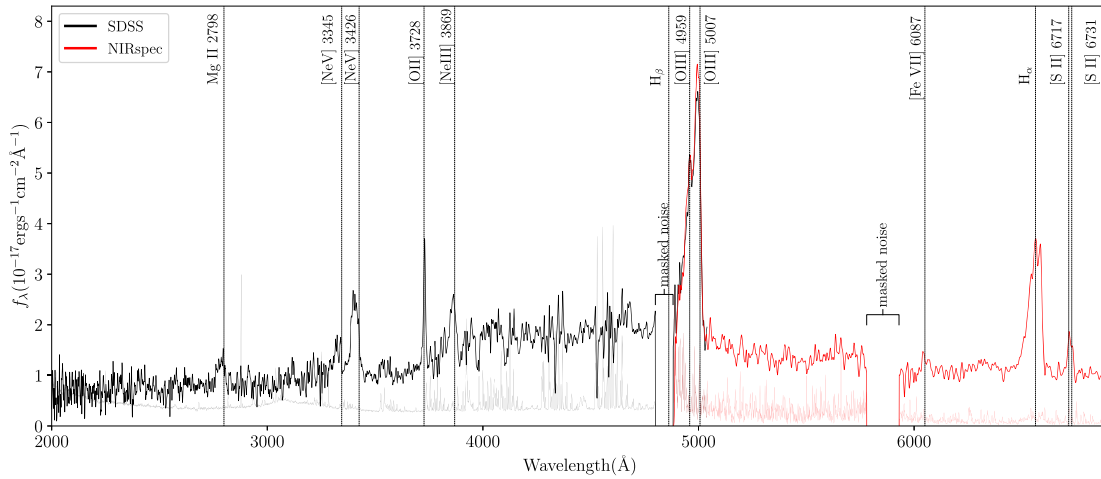
Figure 1. Combined rest-frame SDSS BOSS (black) and NIRSPEC (red) spectra of J0048-0046. Prominent emission lines are labeled across the top. The error spectrum for both BOSS and NIRSPEC and runs across the bottom, peaking at regions most affected by sky-subtraction residuals. The wavelength region between 5780 and 5930 Å is masked due to poorly subtracted sky lines.

higher signal-to-noise ratio (S/N) around [Ne V] using the South African Large Telescope (SALT) Robert Stobie Spectrograph (RSS; Kobulnicky et al. 2003) (2015-1-SCI-020, P.I.: C. Tremonti). The observation was carried out in long-slit mode on 2015 August 8 with seeings of 1.″3–1.″5. We used the RSS PG1300 grating with a 28° tilt angle, which provides a resolving power of $R \sim 2200$ for our observed wavelength range of 6325 and 8148 Å (3260–4200 Å in the target's rest frame). Six exposures of J0048-0046 were taken with the RSS at 1140 s each. Gain correction, bias correction, and mosaicking of these exposures were performed by the SALT data reduction pipeline (Crawford et al. 2010) and further reduced using PyRAF. Wavelength calibration solutions as a function of pixel positions were found by identifying lines of an xenon arc lamp. These solutions were subsequently applied to each exposure. Cosmic ray removal and background subtraction were performed for each exposure. They were then median combined into one 2D spectrum. We then applied extinction correction, aperture extraction, and a heliocentric correction to obtain our final 1D spectrum.

2.1.3. Keck/NIRSPEC

Spectra were obtained with the Near Infrared Spectrometer (NIRSPEC; McLean et al. 1998) on board the Keck II telescope on 2013 September 15 and 17. We used the NIRSPEC filters 1 and 3 corresponding to the Y and J bands to obtain spectral coverage from 0.95–1.35 μm, which includes the [O III] $\lambda\lambda5007, 4959$ and Hα lines in the quasar's rest frame. We used the 0.″76 × 42″ long slit for a spectral resolution of $R = 2000$ or 150 km s^{-1}. A series of 8×300 s in the NIRSPEC-1 filter and 12×300 exposures in the NIRSPEC-2 filter were taken at two different positions along the slit, employing the standard ABBA slit nodding pattern.

The REDSPEC[9] IDL package was used to make spatial and spectral corrections to the raw data. The exposures were dark subtracted and flat-fielded using an internal flat-field calibration lamp. Sky subtraction was preformed by subtracting A-B pairs. We performed relative flux calibrations and telluric absorption corrections using spectra of standard stars observed the same night. The wavelengths are calibrated to the vacuum

heliocentric system using spectra of internal arc lamps. Following standard pipeline produces, we extracted calibrated spectra, which were averaged to produce a final spectrum. The standard deviation was used to create a final error spectrum. Absolute flux calibration was not possible due to variable cloud cover. We therefore scale the NIRSPEC spectrum to match the SDSS spectrum in the 5030–5290 Å region in the rest frame which is free of emission lines. The SDSS and NIRSPEC data both cover the [O III] $\lambda\lambda4959, 5007$ emission lines; the agreement between the two spectra is excellent (see Figure 1). Analysis of the co-added two-dimensional spectrum does not reveal any spatially extended [O III] $\lambda\lambda4959, 5007$.

2.2. SDSS and WISE photometry

J0048-0046 is positioned within the SDSS Stripe 82 region (S82), a 300 deg^2 region on the celestial equator that was repeatedly imaged in the $ugriz$ filters to create a unique database for studying variability (see Abazajian et al. 2009). We use 11 epochs of the photometric data products output from the official SDSS data release images, with the latest being from Data Release 16 (DR16). Hereafter, we refer to all 11 epochs as DR16. These data are reduced using the SDSS photometric pipeline (Lupton et al. 2001; Stoughton et al. 2002) and the product is located on CAS[10], which provides an SQL interface for obtaining product data.

To extract morphological parameters and constrain parameters for proper variability analysis, we utilize the deep co-add images of the S82 database from Fliri & Trujillo (2016), which reach 3σ values of 24.2, 25.2, 24.7, 24.3, and 23.0 mag in the $ugriz$ filters. Since the S82 co-adds are on average four magnitudes deeper than individual SDSS images, we apply our own photometric analysis to these co-adds of J0048-0046 and its neighboring galaxy (Figure 5) using GALFITM (Vika et al. 2013), a photometric-fitting code with its core procedures inherited from the GALFIT package Peng et al. 2002. GALFITM incorporates the ability to fit morphological parameters as a function of wavelength, which is useful for our available multiband images.

Our analysis provides us with an estimate of the effective radius (R_{50}) of J0048-0046 to be compared with the subsample

---

[9] https://www2.keck.hawaii.edu/inst/nirspec/redspec.html

[10] http://skyserver.sdss.org/CasJobs/SubmitJob.aspx

of Hubble Space Telescope (HST)-imaged ERQs from Zakamska et al. (2019). Point-spread function (PSF) images for the field are provided by Fliri & Trujillo (2016), which are input to GALFITM and are incorporated by the program before the model fitting is performed. Sigma images are created in-house by GALFITM through retrieval of the FITS header keys EXPTIME, GAIN, and NCOMBINE (set to 303). We fit J0048-0046 with both a PSF and a Sérsic model simultaneously, whereas we fit the companion galaxy with a Sérsic model only. Morphological fitting parameters, including the sources' effective radii (R50), Sérsic indices, axis ratios, and position angles are fit as a quadratic function of wavelength, while source Sérsic/PSF magnitudes and centroids are allowed to freely vary. Initial values are informed from the SDSS DR16 photObj table. GALFITM performs the fitting on both J0048 and the companion simultaneously using the Levenberg–Marquardt minimization algorithm.

Since the companion galaxy's centroid is only $\sim$2 arcseconds away from that of J0048-0046, it is possible that nightly changes in seeing affect the SDSS pipeline's deblending of the two sources; flux measurements of J0048-0046 could see some epochs including contaminating light from the companion. We perform additional photometric analysis on the 11 SDSS data release images of J0048-0046 and the companion in each of the *griz* bands. We follow the same method using GALFITM as applied to the S82 co-add, however we only fit a Sérsic model to J0048-0046 and neglect the PSF model as the low S/N in some of the images causes issues with parameter degeneracy (specifically in the magnitudes and centroids) when using both Sérsic and PSF models. The starting parameters for the Sérsic models of J0048-0046 and its companion are informed by the S82 co-add results. For each epoch, we follow the prescription of Anderson & King (2000) and its Python implementation from Bradley et al. (2021) to construct PSF images from high S/N stars in the same field as J0048-0046. The best-fit GALFITM model parameters for J0048-0046 and its companion are listed in Table 2.

The Wide-field Infrared Survey Explorer (WISE; Wright et al. 2010) provides infrared magnitudes in filters centered at 3.4, 4.6, 12, and 22 μm (hereafter, W1, W2, W3, and W4, respectively.) These data are used to construct the SED of J0048-0046 (Section 3.2) and to calculate its bolometric luminosity (Table 1). We utilize photometry from the unWISE co-adds (Lang 2014), which provide better resolution and S/N than the original co-add images. We note that the minor axis FWHMs of the four filters range from 5″6–11″65 meaning that J0048-0046 and its neighboring galaxy $\sim$2″ away (Figure 5) are not resolved separately. However, in Section 3.2, we show that the bluer and less luminous companion (in the *u, r,* and *z* bands) galaxy is unlikely to be contributing more than $\sim$5% of the flux in the WISE bands. WISE luminosities were calculated by first converting the reported Vega magnitudes to flux densities and using the appropriate color corrections (Wright et al. 2010). The WISE W1-W4 data reported in Table 1 were obtained in the middle of 2010. Multiyear detections in the W1 and W2 bands are also available from late-2013 until late-2018 through the NEOWISE survey (Mainzer et al. 2011), providing a time-series data set that we use to investigate IR variability in J0048-0046.

Table 1
J0048-0046 Optical, Infrared, and Radio Properties

Name	Wavelength	$\log_{10}(L)$ (erg s^{-1})	EW Å	$\log_{10}(L_{\rm bol})$ (erg s^{-1})
Mg II	2798 Å	$41.92^{+0.31}_{-1.25}$	19.2 ± 17.1	$\cdots$
[Ne V]	3345 Å	$42.01^{+0.34}_{-0.63}$	22.7 ± 27.9	$\cdots$
[Ne V]	3426 Å	$42.44^{+0.21}_{-0.42}$	62.9 ± 39.2	$46.39^{+0.21}_{-0.42}$
[O II]	3728 Å	$42.15^{+0.16}_{-0.26}$	28.6 ± 13.19	$\cdots$
[Ne III]	3869 Å	$42.08^{+0.37}_{-0.45}$	16.7 ± 22.6	$\cdots$
[O III]	5007 Å	$43.17^{+0.16}_{-0.24}$	221.6 ± 32.8	$46.43^{+0.22}_{-0.30}$
Hα	6562 Å	$42.89^{+0.16}_{-0.22}$	123.2 ± 21.3	$\cdots$
W1	3.4 μm	$44.97^{+0.01}_{-0.01}$	$\cdots$	$\cdots$
W2	4.6 μm	$45.26^{+0.01}_{-0.01}$	$\cdots$	$\cdots$
W3	12 μm	$45.66^{+0.02}_{-0.02}$	$\cdots$	$46.59^{+0.05}_{-0.06}$
W4	22 μm	$45.93^{+0.03}_{-0.03}$	$\cdots$	$46.65^{+0.05}_{-0.07}$
FIRST	1.435 GHz	$41.03^{+0.04}_{-0.04}$	$\cdots$	$\cdots$

Note. Luminosities, emission line equivalent widths, and bolometric luminosities calculated from SDSS+NIRSPEC, WISE, and FIRST. Properties of the [O III] doublet, [Ne V], and Hα are calculated using the combined best-fit profiles (see Section 3.1).

2.3. Other Photometric Data

Other sources of photometric data were obtained to further study the presence of optical variability in J0048-0046 and to complete its SED.

The Panoramic Survey Telescope and Rapid Response System (Pan-STARRS1-PS1; Chambers et al. 2016) Data Release 2 extends our catalog of optical photometry for our SED in the *grizy* passbands. Data was obtained using the MAST CAS SQL[11] interface, extracting dates, Kron magnitudes, their respective errors, and photometric flags. While multiple epochs of data are taken of J0048-0046, they are sparse and do not meet our requirements for accurate variability analysis.

For the purpose of classifying J0048-0046 as either radio quiet or radio loud and in order to draw a connection to ionized outflows, we use a radio flux density measurement at 1435 MHz provided by the FIRST (Becker et al. 1995) survey, which utilized the NRAO Very Large Array.

Additionally, we construct a more complete baseline for our SED by utilizing photometric data in the UV and near-IR. NASA's Galaxy Evolution Explorer (GALEX; Martin et al. 2005) provides one epoch of ultraviolet data in the FUV ($\lambda = 1258$ Å) and the near-UV (NUV; $\lambda = 2310$ Å). The images have FWHMs of 4″2 and 5″3 in the FUV and NUV, respectively, and therefore, light from the companion galaxy 2″ away will contribute a fraction of the observed flux. We consider this further in Section 3.2.

The United Kingdom Infrared Telescope Deep Sky Survey (UKIDSS; Lawrence et al. 2007) provides fluxes from its Wide Field Camera (Casali et al. 2007) in the *Y* ($\lambda = 1.03$ μm), *J* ($\lambda = 1.25$ μm), *H* ($\lambda = 1.63$ μm), and *K* ($\lambda = 2.20$ μm) filters. Measurements of total magnitudes for extended sources are problematic in the UKIDSS public catalogs. We therefore use the APER3 magnitudes corrected following the procedure outlined in Bundy et al. (2015).

---

[11] https://catalogs.mast.stsci.edu

Table 2
GALFITM Parameters

Filter	Object	Model	Flux mag	R_e "	Sérsic Index	b/a	P.A. deg
u	J0048	PSF	23.40 ± 0.05	...	...	...	...
g	J0048	PSF	23.28 ± 0.05	...	...	...	...
r	J0048	PSF	22.32 ± 0.05	...	...	...	...
i	J0048	PSF	21.54 ± 0.05	...	...	...	...
z	J0048	PSF	20.70 ± 0.05	...	...	...	...
u	J0048	Sérsic	23.60 ± 0.05	0.07 ± 0.10	1.69 ± 2.52	0.91 ± 0.39	58.55 ± 30.59
g	J0048	Sérsic	23.23 ± 0.05	0.30 ± 0.05	1.52 ± 1.33	0.62 ± 0.20	42.35 ± 16.03
r	J0048	Sérsic	22.27 ± 0.05	0.66 ± 0.04	1.29 ± 0.47	0.40 ± 0.06	25.25 ± 5.22
i	J0048	Sérsic	21.49 ± 0.05	1.11 ± 0.06	1.06 ± 0.32	0.31 ± 0.03	11.15 ± 2.52
z	J0048	Sérsic	20.65 ± 0.05	1.71 ± 0.1	0.79 ± 0.31	0.32 ± 0.05	-1.65 ± 3.46
u	Neighbor	Sérsic	23.70 ± 0.04	0.51 ± 0.06	3.05 ± 1.03	0.14 ± 0.18	-57.09 ± 9.51
g	Neighbor	Sérsic	22.24 ± 0.04	0.52 ± 0.02	1.92 ± 0.43	0.58 ± 0.05	-49.08 ± 5.05
r	Neighbor	Sérsic	21.71 ± 0.04	0.57 ± 0.03	0.94 ± 0.22	0.78 ± 0.05	-48.01 ± 4.97
i	Neighbor	Sérsic	21.50 ± 0.04	0.59 ± 0.03	0.36 ± 0.28	0.65 ± 0.05	-55.59 ± 4.81
z	Neighbor	Sérsic	21.88 ± 0.04	0.61 ± 0.10	0.14 ± 0.91	0.15 ± 0.21	-73.25 ± 7.62

Note. Best-fit GALFITM parameters for J0048 and its neighboring galaxy, applied to the S82 co-add *griz* images. Column

To display a color image of the field surrounding J0048-0046 (Figure 6), we use publicly available data from the Dark Energy Camera Legacy Survey (DECaLS) of the SDSS Equatorial Sky Data Release 8 (PIs: D. Schlegel and A. Dey), observed by the Dark Energy Camera (Flaugher et al. 2015) and part of the 14,000 deg^2 DESI Legacy Imaging Surveys (Dey et al. 2019). Data consist of observations in the *grz* optical bands with depths of at least $g = 24.0$, $r = 23.4$, and $z = 22.5$ mag, 1–2 mag deeper than SDSS photometry.

2.4. Bolometric and Radio Luminosity

Calculating the bolometric and radio luminosity of J0048-0046 is necessary to get a complete view of the radiative and mechanical power of this source, and understand how this source compares to the full population of quasars as specified by the quasar luminosity function. We use a combination of infrared and optical data to estimate the bolometric luminosity of J0048-0046 and the FIRST radio flux density for the radio luminosity. Our adopted cosmological parameters (Section 1) with the estimated redshift are used to infer the luminosity distance to J0048-0046.

The infrared flux values from the WISE W3 and W4 passbands are used to infer AGN bolometric luminosities via the bolometric corrections defined in Runnoe et al. (2012). We follow a procedure for obtaining the W3 and W4 luminosities by first converting the reported Vega magnitudes to flux densities (Jansky). We follow flux conversion methods and color corrections[12] with guidance from Wright et al. (2010). We use the conversion given as

$$F_\nu[\text{Jy}] = \frac{F^*_{\nu 0}}{f_c} \times 10^{-m_\text{vega}/2.5},$$

where $F^*_{\nu 0}$ is the zero magnitude flux density for sources following a power-law spectrum of $F_\nu \propto \nu^{-(2)}$ and f_c is the color correction factor for sources deviating from such a power law ($F_\nu \propto \nu^{-(\alpha)}$). According to our reported W2-W3 and W3-W4 colors, the MIR spectra of J0048-0046 is approximately a

power law with $\alpha = 2$; hence, $f_c = 1$. Additionally, it is reported that a correction to the W4 flux density must be made for steeply rising MIR spectra ($\alpha \geqslant 1$), due to calibration uncertainties. This correction follows as: $F'_\nu[\text{W4}] \approx 0.90 \times F_\nu[\text{W4}]$. We use Equations (6) and (8) from Runnoe et al. (2012) to calculate our source's bolometric luminosity from its W3 and W4 luminosities.

Estimates of AGN bolometric luminosity are also calculated using the [O III] $\lambda 5007$ and [Ne V] $\lambda 3426$ emission lines. We calculate the luminosity of both lines using the combined narrow and broad components of the fits described in Section 3.1. We adopt Equation (3) from Pennell et al. (2017) to compute an [O III] $\lambda 5007$ bolometric luminosity. Since [Ne V] $\lambda 3426$ has a much higher ionization potential than [O III], it is an even better tracer of AGN activity. However, there are no published bolometric corrections for [Ne V]. We instead use the work of Gilli et al. (2010), who computed the relationship between 2 and 10 keV (X-ray) and [Ne V] $\lambda 3426$ using a sample of AGN at $z = 0$–1.5, finding $L_X/L_{\text{Ne V}} \sim 400$. We then utilize luminosity-dependent X-ray bolometric correction of (Duras et al. 2020, their Equation (3)). Taking the median luminosity of the Gilli sample to be $L_{2–10\,\text{eV}} = 44.5$, we find an X-ray bolometric correction of $K_X = 22.12$. Combining this with the $L_X/L_{\text{Ne V}}$ ratio, yields a [Ne V] bolometric correction of 8848. Neither the [O III] nor the [Ne V] bolometric corrections require that the emission lines have been corrected for dust attenuation. In any case, we are unable to determine an accurate attenuation for the NLR with our current data due to large sky residuals near Hβ. We use the host galaxy A_V value of 0.17 calculated in Section 4.2 to correct for attenuation in the NLR and find that [O III] and [Ne V] bolometric luminosities increase by a factor of 1.17, however this estimate is highly uncertain and thus we prefer to consider the uncorrected luminosities.

The bolometric luminosities computed from WISE W3 and W4 and the emission lines of [Ne V] and [O III] are reported in Table 1. The four different tracers yield an average of $\log L_\text{bol} = 46.52 \pm 0.46$, with the emission line luminosities being 0.1–0.2 dex lower than the IR luminosities. This may be

---

[12] http://wise2.ipac.caltech.edu/docs/release/allsky/expsup/sec4_4h.html

due to a small contribution of light from the companion source to the WISE bands. J0048-0046 was included in a sample of IR-bright dust obscured galaxies (DOGs; Toba et al. 2017) whose bolometric luminosities were estimated using SED fitting. They report $\log_{10}(L_{\rm bol}) = 46.26$ erg s^{-1}, slightly lower than the values we find. However, the overall agreement among the various tracers of bolometric luminosity is very good, considering the large amount of scatter seen in the galaxies used to calibrate bolometric corrections (± 0.3 dex; Duras et al. 2020).

Using the bolometric luminosity calculated from the [O III] band, we compare to the QLF from Shen et al. (2020) (see Figure 4 in their work) and find that J0048-0046 is ~ 3 times more luminous than a typical quasar at $z = 1$. We also note that J0048-0046 is slightly less luminous than the median bolometric luminosity of core ERQs ($\log_{10}(L_{\rm bol}) \sim 47.1$ erg s^{-1}) which were estimated using the W3 band.

We compute the radio luminosity of J0048-0046 using the FIRST reported flux density at a central observed-frame frequency of $\nu_{\rm obs} = 1.435$ GHz. Following Hwang et al. (2018), we calculate the radio luminosity as

$$\nu L_\nu = 4\pi D_{\rm L}^2 (1+z)^{-1-\alpha} (\nu/\nu_{\rm obs})^{1+\alpha} \nu_{\rm obs} F_{\nu_{\rm obs}}, \quad (1)$$

where the k-correction is applied to the rest-frame frequency, $\nu = 2.77$ GHz, of J0048-0046 and a spectral index of $\alpha = -0.7$ is assumed. $F_{\nu_{\rm obs}}$ is the observed flux density and $D_{\rm L}$ is the luminosity distance calculated using our assumed cosmological parameters.

The radio luminosity is reported in Table 1. The threshold for an ERQ to be considered radio loud is estimated by Hwang et al. (2018) to be $\nu L_\nu [5\,\text{GHz}] > 10^{41.8}$ erg s^{-1} given their average [O III] luminosity (Xu et al. 1999). This threshold criterion establishes J0048-0046 as a radio-quiet AGN.

3. Spectral Analysis

3.1. Emission Lines

We display the BOSS and NIRSPEC spectra jointly in Figure 1. Upon initial visual inspection of the BOSS spectrum, it is apparent that the optical light of J0048-0046 is composed of two main components. The continuum light of J0048-0046 is dominated by starlight from the host galaxy (discussed in detail in Section 4.2). On top of this strong host galaxy continuum are emission lines typical of Type 2 AGN, specifically [Ne III] $\lambda 3869$, [Ne V] $\lambda\lambda 3345, 3426$, and [O III] $\lambda\lambda 4959, 5007$. Due to sky noise at 4861 Å, we are not able to comment on the line profile of Hβ in our SDSS spectrum and Hα is heavily blended with [N II]. However, we do see Mg II $\lambda 2798$, a line that is typically broad in Type 1 AGNs. While Mg II is highly broadened (FWHM ~ 36 Å), it does not show the classical Lorentzian shape common in Type 1 AGN, rather it appears to have a similar velocity structure to the lines associated with the NLR. This is similar to core ERQs, where the UV broad emission lines (e.g., N V, S IV, and C IV) are found to lack broad wings. Hamann et al. (2017) suggest that these unusual line kinematics are the result of outflows and spatially extended BLRs that may connect to the low-density forbidden line regions farther out.

There are peculiarities present in the NLR of J0048-0046 that are apparent with an initial visual inspection of Figure 1. One of these peculiarities is the strong blueshift and broadening in the NLR (Figures 1 and 2). In fact, this causes [O III] $\lambda 5007$
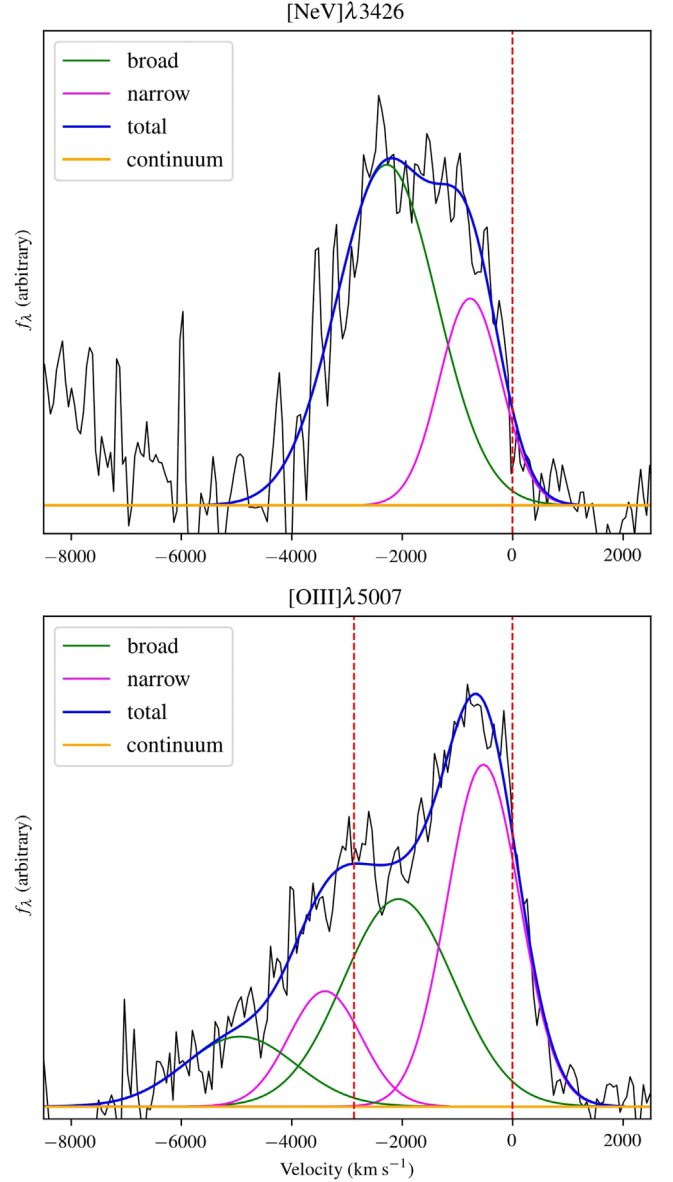
Figure 2. Velocity profile of [Ne V] $\lambda 3426$ from the SALT spectrum and [O III] $\lambda 5007$ from the BOSS spectrum. The red line indicates the emission lines' rest-frame zero velocity. The y-axis is in arbitrary units of flux since we are not able to flux calibrate with the SALT data.

to blend with [O III] $\lambda 4959$. In contrast, the [O II] $\lambda 3728$ is narrow (FWHM ~ 7 Å) and shows no blueshift to its centroid. We use the multicomponent fitting method described in Perrotta et al. (2019) to decompose the line profile and calculate w_{90} and v_{98} of [O III] and [Ne V]. The w_{90} parameter is a measure of the velocity interval containing 90% of the line flux, excluding the most blue/redshifted regions of the line. The v_{98} parameter is measured as 98% of the line flux from positive velocities to negative velocities with respect to the systemic redshift. It can thus be thought of a near-maximum estimate of the outflow velocity. To estimate the error on w_{90} and v_{98}, due to uncertainties in the fit, we consider the best-fitting parameters uncorrelated, vary them in a range of $\pm 1\sigma$, and calculate the resulting change in w_{90} and v_{98}. We adopt the maximal variation of these values as an upper limit error with typical value of 200–300 km s^{-1}. An additional fit is performed on the Hα+[N II] emission by allowing a varying broad Hα
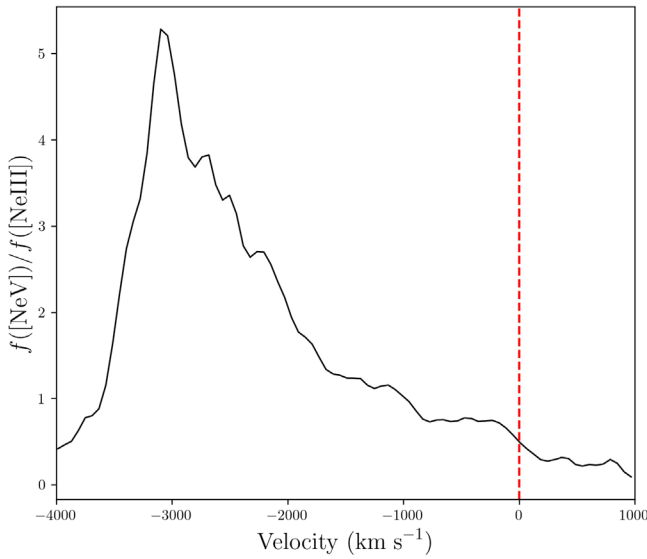
Figure 3. Continuum-subtracted flux ratio of [Ne V] λ3426 to [Ne III] λ3869 from the BOSS spectrum smoothed by a 10 pixel boxcar. Both emission lines have been transformed to velocity space based on their respective center wavelengths.

component while assuming a 1:3 ratio between the two [N II] features, along with fixed-width narrow components set equal to that of [O II] (7 Å), therefore giving us a cleaner estimate of the Hα luminosity and equivalent width (EW) for Table 1.

The retrieved w_{90} of [O III] is 4008 ± 378 km s^{-1}, very close to the median w_{90} of 4050 km s^{-1} for the core ERQs. We retrieve an [O III] v_{98} of -4095 ± 423 km s^{-1}, slightly more blueshifted than the core ERQ median of -3528 km s^{-1}. The line fitting for [Ne V] yields a w_{90} of 3469 ± 300 km s^{-1} and a v_{98} of -4013 ± 300 km s^{-1}. Similarities in both parameters between the two lines suggests that they are likely part of the same outflow. The REW of [O III] λ5007 is 218 Å, approximately 100 Å higher than the median REW of the Perrotta et al. (2019) sample, which is partially driven by the relatively faint continuum.

Another indicator of quasar feedback observed in J0048-0046 is the atypical emission line ratios of the NLR. We report emission line luminosities in Table 1. We correct for foreground Milky Way dust attenuation but do not correct for attenuation intrinsic to the source, as the S/N in the region of Hβ is too low. For comparison, we use the reported line ratios of the Type 2 quasar spectrum from Zakamska et al. (2003). The ratio of [O III] λ5007/[O II] λ3727 is 6.7 in J0048-0046 compared to 1.8 from the Type 2 composite. Additionally, the ratio of [Ne V] λ3426/[Ne III] λ3869 is 2.95, whereas in the Type 2 composite it is 0.68. When considering the profile of the [Ne V] to [Ne III] ratio (Figure 3), we find that higher outflow velocities have higher [Ne V]/[Ne III], indicating a link between the outflow and the ionization state of the gas. [Ne V] is an excellent indicator of AGN activity given its high ionization potential of 97 eV (Gilli et al. 2010); however, this line can also arise from photoionization by Wolf-Rayet stars found in young starbursts (Abel & Satyapal 2008). Such starbursts have been observed to be young ($\sim$3 Myr) with extreme SFR surface densities ($\Sigma_{SFR} \approx 3000\ M_{\odot}$ yr^{-1} kpc^{-1}; Sell et al. 2014). Given the many signs of AGN activity in J0048-0046 and a lack of a powerful starburst (see Section 4.2),

we infer that [Ne V] predominantly traces AGN activity in this source.

3.2. Broadband Spectral Energy Distribution

Photometry over a wide baseline of wavelengths contribute to the SED of J0048-0046: GALEX, SDSS Pan-STARRS1, UKIDSS, and WISE photometric measurements (Section 2) build the quasar's spectral shape from the FUV to the IR. In Figure 4, we compare the SED of J0048-0046 to the SEDs of several types of quasars. We use a Type 1 QSO composite template from Polletta et al. (2008) and a Type 2 QSO template from Hickox et al. (2017).

As noted in Section 2, the apparent merging companion of J0048-0046 cannot be deblended in the WISE and GALEX data and likely contributes to the observed flux at these wavelengths. In Figure 4, we show the fluxes of J0048-0046 and the companion in the SDSS bands as green circles and red stars, respectively; the sum of the two fluxes is shown as magenta stars. The companion's z band flux ($\lambda_{rest} \sim 4600$ Å) is only 22% that of J0048-0046 and it is undetected the UKIDSS *YJHK* bands. In addition, it is 0.5 mag bluer in $g - i$ suggesting that it is lower mass and less dusty. To quantify the companion's potential contribution to the WISE and GALEX bands, we use the `Prospector` code (Leja et al. 2019; Johnson et al. 2021) to fit the galaxy's SDSS photometry and to predict its full SED. The code models both the stellar light and dust reprocessed emission. We use the same models and priors used in Davis et al. (submitted) and we assume the companion is at the same redshift as J0048-0046 on account of the tidal bridge between the two (Figure 5). `Prospector` employs a gridless, Bayesian parameter estimation with the incorporation of robust posterior sampling algorithms. We randomly draw models from the probability distribution function and synthesize their GALEX and WISE magnitudes. Taking the 84th percentile of the simulated magnitude distribution, we compute the potential contribution of the companion to the flux in each band. The GALEX FUV samples wavelengths below the Lyman break, so the contribution is negligible; in the NUV it is <7%. In the WISE bands the companion contributes 4% in W1, 1% in W2, 0.5% in W3, and 0.1% in W4 to the total flux. Nonetheless, it may be most appropriate to consider the SED of the merging pair, which is shown as the dashed black line.

Figure 4 shows that J0048-0046 has a dramatically different spectral shape than a typical Type 1 QSO and a Type 1 QSO behind a Calzetti et al. (2000) dust-reddening screen with $E(B - V) = 1$. There is a strong deviation in overall spectral shape which becomes particularly severe at wavelengths less than 6000 Å. This demonstrates that J0048-0046 is not consistent with being a typical Type 1 quasar seen behind an unusually large dust-reddening screen.

The Type 2 QSO template is a reasonably good match to our source's SED at optical wavelengths on account of the significant starlight contribution in J0048-0046 (Section 4.2). However, the Type 2 template is relatively flat at wavelengths redder than 0.5 μm, whereas the flux of J0048-0046 increases by nearly an order of magnitude. The notable bump in our sources SED around 0.45 μm is a feature of the starlight (which can be seen more clearly in Figure 7). The [O III] line emission contributes strongly to the Pan-STARRS y band, but emission lines impact the other optical+NIR filters by less than 20%. The prominent 0.45 μm SED bump is evident even when the photometry is corrected for the contribution of emission lines.
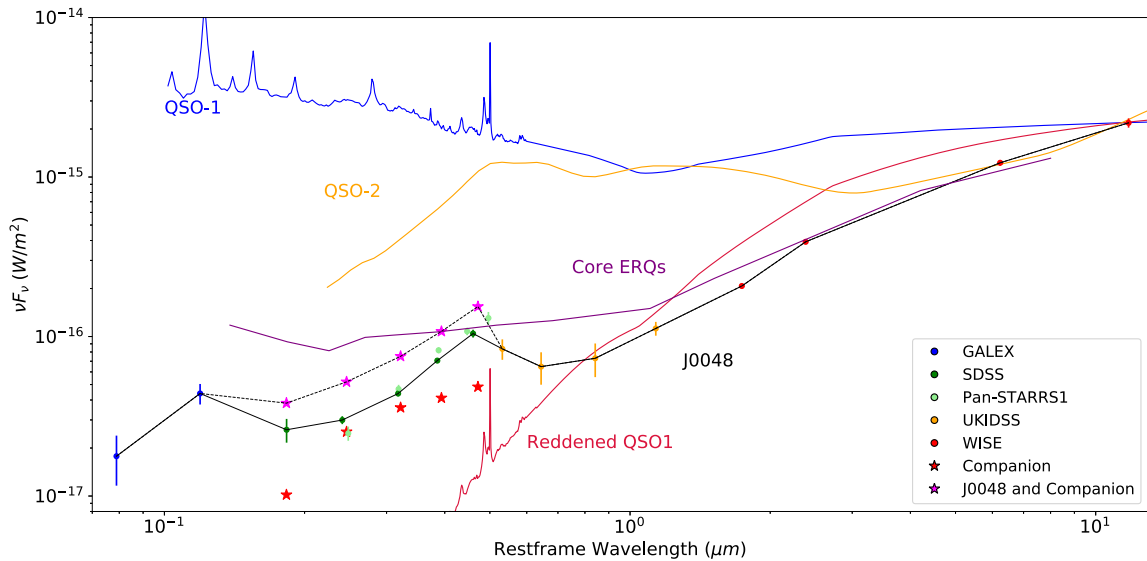
Figure 4. Rest-frame SED of J0048-0046 (black line, colored circles) compared to the core ERQ sample of (Hamann et al. 2017, purple). Type 1 (blue) and Type 2 (yellow) quasar templates from Polletta et al. (2008) and Hickox et al. (2017) are shown for comparison, along with a reddened Type 1 quasar ($E(B-V) = 1$; red). SEDs are normalized to a common value at 10 μm for visualization purposes. The star symbols show the optical SED of the companion galaxy (red) and its combined flux with J0048-0046 (magenta). The two galaxies are unresolved in the WISE and GALEX bands (see Section 3.2). The SED of J0048-0046 is most similar to the SED of the core ERQs. However, it is somewhat redder and it shows a bump at 0.45 μm, due to the contribution of starlight to the SED.

The importance of emission lines to the broadband SED may be greater in the UV with the bump near 0.12 μm potentially arising from Lyα + N V λ1240.

The SED of J0048-0046 is most similar to the SED of the core ERQs of Hamann et al. (2017). In particular, the SED rises strongly above 1 μm, indicating a a heavily obscured AGN, but is surprisingly flat below 1 μm compared to the expectation of a simple *foreground screen* dust reddening. This unusual SED shape could arise due a clumpy dust distribution where some of the UV light is completely absorbed and re-radiated in the IR and some is transmitted along less attenuated sightlines. It is evident that our source is slightly more reddened than the core ERQ sample; however, it is well within the scatter of the individual core ERQ SEDs as shown in Figure 16 of Hamann et al. (2017). The primary difference in the SEDs is the bump near 0.45 μm, which suggests that the optical spectrum of J0048-0046 is dominated by starlight. It is possible that our source may be a Type 2 ERQ (see Ross et al. 2015 for some additional examples of Type 2 ERQs.) In this case, some of the UV light might be due to dust scattered QSO continuum. Alternatively, it could be a Type 1 ERQ where the QSO continuum that does penetrate a clumpy dust distribution is much more heavily reddened than the host galaxy, allowing the latter to dominate.

The rest-frame ultraviolet to MIR color of J0048-0046 is $i - W3 = 5.2$ mag (AB), meeting the threshold of $i - W3 > 4.6$ mag employed by Hamann et al. (2017). We calculate that this color would be $i - W3 = 6.5$ mag if J0048-0046 were at the median core ERQ redshift ($z = 2.5$), consistent with the overall redder SED profile of J0048-0046.

the host galaxy of a candidate ERQ. In Figure 5, we show the deep *ugriz* S82 co-add images (Fliri & Trujillo 2016) of J0048-0046 and its neighboring galaxy. The median PSF FWHM is $\sim$1$\farcs$1; therefore, we cannot resolve substructure smaller than $\sim$8.7 kpc, limiting our analysis to very basic properties.

The most notable feature of the S82 co-add image, shown in Figure 5, is the existence of a lower luminosity source to the southwest of J0048-0046; the apparent bridge-like structure between the two indicates that it may be a merging companion. However, we acknowledge the possibility that this apparent companion is simply a background source. The companion galaxy is 2$\farcs$5 from J0048-0046, and was not included in the SDSS 2$''$ diameter fiber spectrum, so we have no information on its redshift at present.

Resultant magnitude values from our GALFITM analysis of the S82 co-add (Section 2.2) for both sources are reported in each panel of Figure 5. We obtain a g-band R_{50} value of $(0.30 \pm 0.05)''$ or (2.42 ± 0.40) kpc for J0048-0046 and $(0.52 \pm 0.05)''$ or (4.20 ± 0.1) kpc for the neighbor. The quoted errors are purely statistical (Peng et al. 2002) and do not reflect the uncertainty of our PSF model. The R_{50} of J0048-0046 is roughly a factor of 2 lower than the average R_{50} from the 10 ERQs with HST-imaged host galaxies (Zakamska et al. 2019).

In Figure 6, we show a larger DECaLS color image centered on J0048-0046. The companion appears significantly bluer than J0048-0046. Indeed, the SDSS ($g - i$) colors are 1.5 and 1.0 for J0048-0046 and the companion, respectively. The DECaLS image does not show any hints of a surrounding larger scale structure such as a galaxy cluster or massive group.

4. Host Galaxy Analysis

4.1. Morphology

The optical spectrum of J0048-0046 (Figure 1) appears to be dominated by starlight (see Section 4.2 for a quantitative analysis). This provides us with a unique opportunity to study

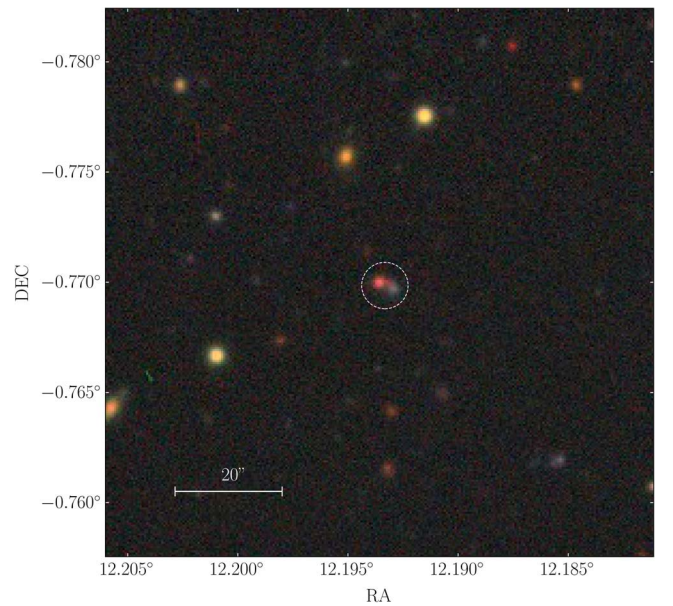### 4.2. Stellar Mass and Star Formation History

The fact that J0048-0046 is dominated by host galaxy light presents us with a rare opportunity to investigate the stellar population of an ERQ host. We fit the combined SDSS and NIRSPEC spectrum with stellar population synthesis models. We use simple stellar population (SSP) models generated with
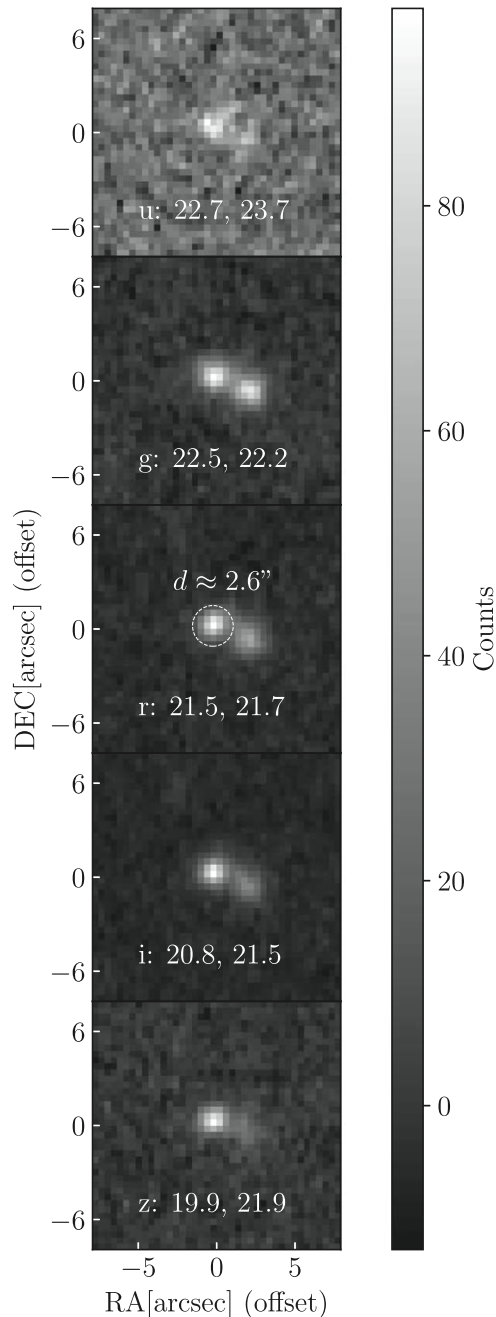
Figure 5. SDSS *ugriz* images of J0048-0046 from the Fliri & Trujillo (2016) Stripe 82 co-addition. J0048-0046 is encircled in the *r*-band image. The fainter source to the southwest of J0048-0046 is a possible merging companion, as indicated by the apparent tail-like structure between the two galaxies. In each panel, numbers are the computed magnitudes from GALFITM for J0048-0046 (left) and the companion (right) (see the Appendix). The quoted magnitudes for J0048-0046 are the combination of its fitted Sérsic and PSF magnitudes. The *ugriz* filters probe rest-frame wavelengths of 1830, 2410, 3180, 3860, and 4600 Å, respectively.


Figure 6. Color image from a combination of the DECaLS *grz* images (Dey et al. 2019) showing the larger scale environment of J0048-0046. J0048-0046 and its possible companion are encircled in the center.

the Flexible Stellar Population Synthesis code (Conroy et al. 2009; Conroy & Gunn 2010) using Padova 2008 isochrones, a Salpeter (1955) IMF, and a new theoretical stellar library "C3K" (C. Conroy et al., 2022, in preparation) with a resolution of $R \sim 10{,}000$. Because the S/N of our spectrum is low (~ 3 per pixel), we utilize a fairly sparse model grid, consisting of 12 solar metallicity SSPs with ages of 1, 5, 25, 100, 200, 315, 400, 500, 630, 1000, 2000, and 5600 Myr.

(At $z = 0.94$ the universe is roughly 6.1 Gyr old.) We convolve our template spectra to SDSS resolution ($R \sim 2000$) and then further convolve them to the galaxy's velocity dispersion, which we vary between $\sigma = 100$–200 km s^{-1}.

Because our spectrum contains a mix of quasar and galaxy light, we also include a Type 1 quasar template from Polletta et al. (2008). The quasar template was built from a combination of photometry and spectroscopy with the spectroscopic portion of the template extending to 6000 Å. We patch the template at wavelengths of 6000–7250 Å with an SDSS quasar composite spectrum that we generated by selecting and stacking the spectra of high luminosity quasars ($\log L_{3000} > 45$) drawn from the Shen et al. (2011) quasar catalog. Since the Hα line is masked out of our fit, the motivation for the patch is primarily esthetic, when comparing the quasar and host galaxy light contributions (see Figure 7).

In our model, the stellar populations and the quasar experience different dust attenuation. For the stellar populations, we use a dust attenuation curve appropriate for massive high-z galaxies from Salim et al. (2018). For the quasar, we use the AGN attenuation curve derived by Gaskell & Benker (2007), which lacks a 2200 Å bump and is flatter than the curve we use for the host galaxy.

After carefully masking regions of bad data and emission lines, we fit the model to our data using a custom built IDL code which is based on the mpfitfun routine (Markwardt 2009). The model returns the fraction of light contributed by each template (SSPs, QSO) at 5500 Å and the reddening applied to the starlight and QSO light. The fit is carried out over the full wavelength range of our SDSS + NIRSPEC spectrum, which is 2000–7000 Å in the galaxy's rest frame. We considered including photometric data in our fit to extend the wavelength baseline, but our dust model is too simple (a foreground screen) and we do not model dust emission which would be required to reproduce the IR SED. To insure that the fit does not get stuck in a local minimum, we run our code 500 times with the starting parameters of the fit and the
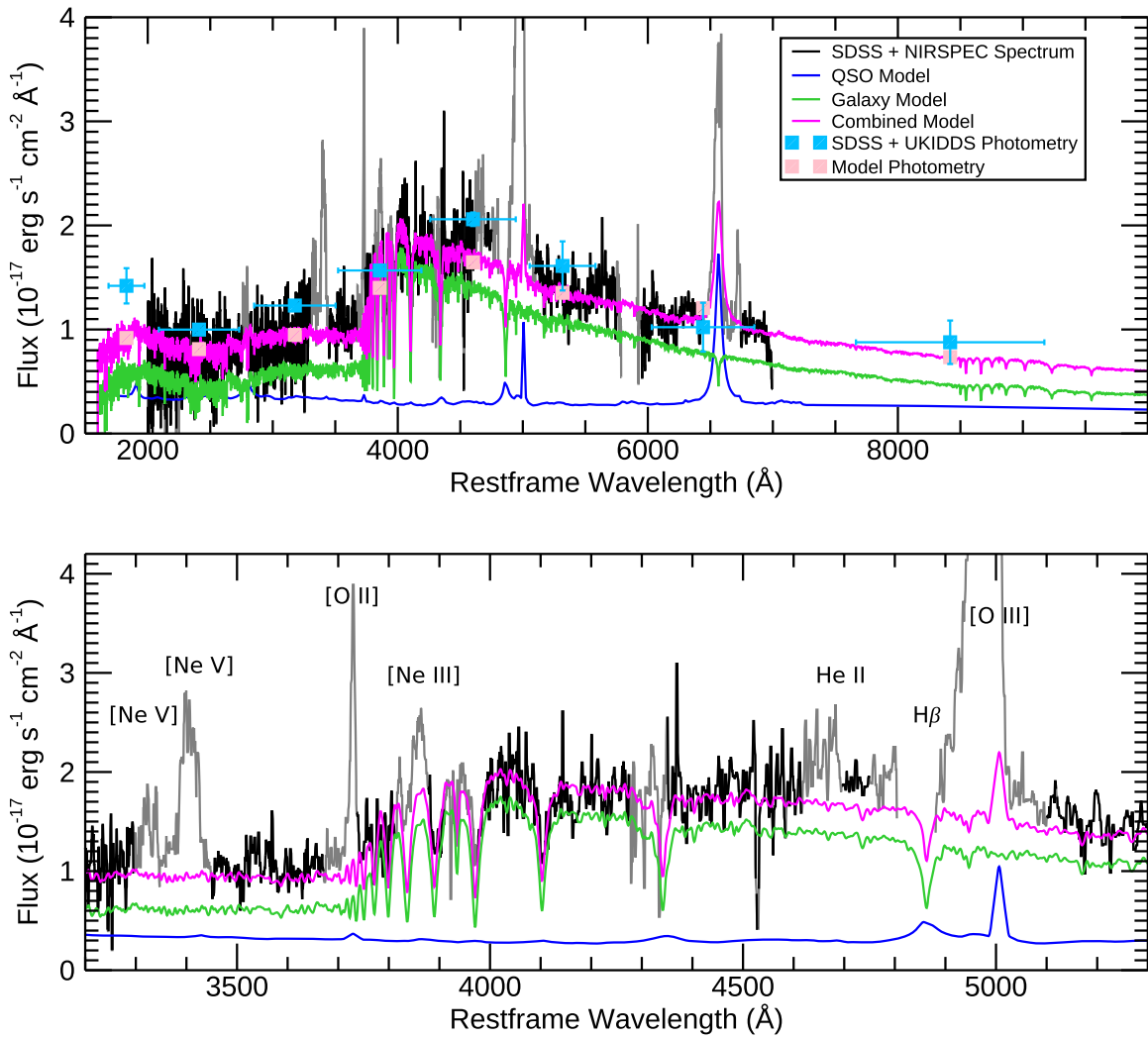
Figure 7. Combined SDSS and NIRSPEC spectrum (black) with the best-fit stellar population synthesis model overlaid (magenta). Regions of the spectrum that are masked out of the fit are shown in gray. The best-fit model is made of a lightly attenuated stellar population (green) and a more heavily attenuated QSO spectrum (blue). Photometric data from the SDSS Stripe 82 co-add (*ugriz*) and UKIDSS (*YJH*) are overlaid (blue points). We have normalized the spectrum to match the SDSS *i*-band photometry. Synthetic photometry of the best-fit model is shown in pink.

velocity dispersion randomly varied. We then adopt the model with the lowest χ^2 as our best fit.

In Figure 7, we show our best-fit models overplotted on the data. The QSO is highly reddened ($E(B-V) = 0.34$, $A_V = 1.76$), while the starlight is minimally reddened ($E(B-V) = 0.06$, $A_V = 0.17$). However, ERQs are known to have a large scattered light contribution in the UV (Alexandroff et al. 2018), and thus the reddening computed for the QSO assuming our simple dust model should not be considered physically realistic. As we discussed in Section 3.2, a simple foreground screen dust model is unlikely to be able to reproduce the UV-IR SED of ERQs. The QSO contributes ~16% of the light at 4000 Å, but more than 35% below the Balmer break and at wavelengths longer than 8000 Å. While it is possible to obtain a good fit to the data without including the QSO template, this increases the reduced χ^2 by 9%.

The stellar population is entirely dominated by a single SSP with an age of 400 Myr, suggesting the host galaxy is a *post-starburst* (see, Wild et al. 2009). Given that our code does not favor the inclusion of 300 or 500 Myr old templates in the fit, we can conclude that the burst had a short duration. If we assume that the stellar mass ascribed to the 400 Myr old

population formed at a constant rate over 100 Myr, it implies a star formation rate of 560 $M_{\odot}$ yr^{-1}, consistent with values found for submillimeter galaxies (see, Dudzevičiūtė et al. 2020).

Whether star formation is truly shutoff at present is difficult to precisely ascertain from SSP fitting because there is some degeneracy between the QSO spectrum and a very young stellar population (e.g., both are relatively featureless and blue over the range of wavelengths considered here). An alternative approach to estimating the SFR in the last 10 Myr is to use the nebular emission lines. In J0048-0046, the Hα line (Figures 1, 7) is broad, blueshifted, and blended with [N II] $\lambda\lambda6548$, 6584; its ionization is likely dominated by the AGN. However, [O II] $\lambda\lambda3726$, 3729 is relatively narrow (FWHM = 7 Å) and appears to trace the host galaxy kinematics, suggesting that it does not arise in the AGN outflow. Unfortunately, [O II] is far from an ideal SFR indicator due to its strong sensitivity to dust and metallicity (Moustakas et al. 2006). To partially account for this, Moustakas et al. (2006) derive calibrations between SFR and $L_{\text{[O II]}}$ (uncorrected for dust) in bins of *B*-band luminosity. The host galaxy of J0048-0046 has $\log(L_B/L_{B,\odot}) = 11.09$, placing it in the highest luminosity

bin defined by Moustakas et al. (2006). Using their SFR calibration and our measured $\log L_{[O\ ii]}$ (Table 1), we find SFR $= 72^{+45}_{-31}\ M_\odot$ yr^{-1}, where the error bars reflect the SFR calibration uncertainty. This should be considered an upper limit on the ongoing SFR, as the [O II] may partly arise from the AGN or from ionization by evolved stars (Yan et al. 2006). Taking the derived numbers for the past and present value of the SFR at face value, we see that star formation has decreased by a factor of 5–14 over the past 400 Myr, even if star formation is still ongoing at some level. This confirms the post-starburst nature of the host galaxy. The Lick Hδ absorption index is 7.2 ± 2.7, consistent with the H$\delta > 5$ criterion adopted by Alatalo et al. (2016) for their sample of shocked post-starbursts.

The spectral fitting algorithm finds a M/L ratio, which suggests a total stellar mass of $5.6 \times 10^{10}\ M_\odot$, assuming a Salpeter (1955) IMF; however, this is likely a lower limit. The fact that our code fails to find evidence of an older stellar population is, in part, due to a tendency of our code to use a minimum number of templates to fit the data. (A similar behavior is present in other stellar population fitting software such as pPXF Cappellari 2017.) If we force our fit to put no more than 50% of the mass at stellar ages $\leqslant 2$ Gyr, we increase the reduced χ^2 by only 1% since the 5.6 Gyr SSP contributes minimally (0.1%–10%) to the total stellar light. With our young/intermediate age population thus limited, the stellar mass increases by a factor of 1.8–$9.8 \times 10^{10}\ M_\odot$, which we take to be our upper limit on the mass. Plugging our plausible range of stellar masses (5.6–$9.8 \times 10^{10}\ M_\odot$) into the Zahid et al. (2016) scaling relation between stellar mass and velocity dispersion, we predict a velocity dispersion of 161–189 km s^{-1}, whereas our measured dispersion is 140 km s^{-1}. However, the starlight in our galaxy is clearly dominated by the young burst, which is likely to be centrally concentrated and more rotation dominated (Mihos & Hernquist 1994; Hopkins et al. 2008, 2009) and thus the measured dispersion may not trace the galaxy's full potential well.

5. Variability

Upon an initial inspection of the optical spectrum of J0048-0046, its prevalent narrow-line emission makes it tempting to classify the source as a Type 2 quasar. Through AGN unification models, it is expected (and observed) that Type 2 quasars show little to no optical variability due to obstruction around their coronal region (Bershady et al. 1998; Sarajedini et al. 2006; Yip et al. 2009). This idea has persisted through a more recent analysis of extreme variability quasars (EVQs; Barth et al. 2014) with $\Delta g \approx 1$, which found that EVQs in Type 2 samples are actually Type 1.8 and 1.9 contaminants. Given that J0048-0046 is not a standard Type 2 quasar (Section 3.2), stellar population modeling favors a QSO contribution to its optical spectrum (Section 4.2), and it is conveniently located in the S82 region (Section 2.2), we are motivated to investigate the source for variability. Moreover, no ERQ to date has been observed with high-cadence, time-series photometry, making J0048-0046 the first ERQ to be investigated for variable properties.

Using the SDSS Data Release 16 (DR16) and NEOWISE data products described in Section 2.2, we construct light curves to inspect for variability in J0048-0046. Note that the SDSS u band is dropped for variability inspection due to its large error bars. An initial examination of the light curve shows
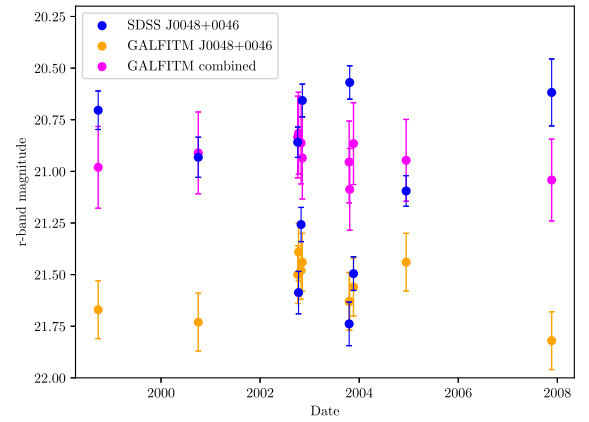
Figure 8. SDSS r-band light curve of J0048-0046 with blue points showing the model magnitudes taken directly from SDSS DR16 photometric catalog and orange points showing the output of GALFITM applied to the DR16 images (Section 2.2). The magenta points show the combined magnitudes of J0048-0046 and its companion as calculated by GALFITM. Variations in the deblending of the two sources by the SDSS photometric pipeline lead to apparent variability in the catalog data. With our more careful treatment of the data using GALFITM, no convincing evidence of variability is found.

that J0048-0046 has strong, short timescale variability in the optical regime. To quantify the variability across different photometric bands, we make use of the fractional variance ($F_{\rm var}$; Vaughan et al. 2003), which calculates the rms variability amplitude as a percentage. When applied to the 11 epochs of the DR16 photometry, we find $F_{\rm var}$ values of $35\% \pm 5\%$ in the g band down to $29\% \pm 4\%$ in the z band.

However, one concern with the SDSS catalog photometry is that sources are modeled and deblended separately at each epoch and differences in the deblending of J0048-0046 and its close companion could masquerade as variability. To explore this, we carry out our own photometry of the 11 DR16 images using GALFITM as described in Section 2.2. Figure 8 shows the original J0048-0046 r-band light curve as queried from SDSS DR16 along with the light curve constructed using GALFITM. The running median of the GALFITM light curve is shifted by $\sim +0.7$ mag when compared to the SDSS DR16 catalog photometry and signs of variability are greatly reduced. Figure 8 also shows the combined light curve of J0048-0046 and its companion; at certain epochs, the combined flux of the two sources is proximal to the DR16 catalog values for J0048-0046, indicating that pipeline deblending issues likely occurred. Since the variation of our GALFITM photometry is less than the computed errors, $F_{\rm var}$ is undefined in each of the four bands, meaning that there is no variability detected at rest frame 0.24–0.46 μm in our relatively shallow data. Since ERQ samples might have high merger rates, any future ground-based photometric studies of ERQs should exercise similar caution when using survey data products. We find that variability is also undetectable for the NEOWISE W1 and W2 light curves ($N = 149$), which probe rest-frame wavelengths of 1.7 and 2.4 μm, respectively.

6. Results and Discussion

Our analysis of the multiwavelength photometry and optical spectra of J0048-0046 conclusively indicates that the source is not a typical Type 1 or 2 quasar, nor is it a Type 1 quasar behind a strong dust-reddening screen. Broad and blueshifted narrow lines ([O III], [Ne V]) with velocities as high as

$-4000 \, \mathrm{km \, s^{-1}}$ suggest that the source's AGN may be powering galactic-scale outflows. In these respects, the J0048-0046 resembles the core ERQs studied by Hamann et al. (2017); however, it is at a lower redshift such that it is easier to study its host galaxy. Below we summarize the defining properties of core ERQs and their likely physical interpretation. We then revisit the key aspects of J0048-0046 that lead us to classify it as an ERQ and discuss notable differences. We highlight the unique aspects of our analysis—the study of the QSOs variability and the host galaxy's stellar population—and we consider how the insights gained from J0048-0046 can shed further light on the nature of ERQs.

6.1. The Nature of Core ERQs

The core ERQ sample defined by Hamann et al. (2017) is selected to have $i - W3 > 4.6$, $z = 2.0$–3.4, and C IV EW > 100 Å. The resulting sample of core ERQs have the following properties:

1. Unusual emission line flux ratios, in particular, large ratios of NV/Lyα, N V/C IV, and Si IV/C IV
2. High EW broad emission lines with unusual wingless line profiles and blueshifted line centroids
3. SEDs that are red in the rest-frame optical-IR but flat/blue in the UV and are, thus, inconsistent with quasars behind a simple dust-reddening screen
4. Ubiquitous powerful ionized outflows traced by [O III] 5007 (Perrotta et al. 2019)
5. Low luminosity radio emission possibly associated with wind-driven shocks (Hwang et al. 2018)
6. High Eddington ratios ($L_{\mathrm{bol}}/L_{\mathrm{Edd}} = 0.22$–$4.03$; Perrotta et al. 2019)
7. Luminous host galaxies ($\log(L_B/L_{B,\odot}) = 10.92$–$12.03$; Zakamska et al. 2019)

Hamann et al. (2017) carefully consider several different models to explain these properties, in particular, the close connection observed between reddening and the unusual emission line properties. They converge on a model where ERQs are luminous quasars with unusually powerful and extended outflows that encompass most of the line-forming regions. In this model, the unusual UV emission line properties are a consequence of outflow-dominated BLRs that are vertically extended above the accretion disk and potentially connected to the high-speed low-density [O III] gas much farther out. The unusual SEDs are explained by patchy obscuration due to small dusty clouds embedded in the outflows. Spectropolarimetric observations of a small sample of ERQs support this general scenario (Alexandroff et al. 2018). While this outflow model emphasizes small-scale phenomena and does not explicitly link the quasars to the evolution of their hosts, it has been suggested that ERQs could represent an transition phase in quasar/host galaxy evolution in which a heavily obscured quasar is blowing out the dusty circumnuclear ISM and quenching star formation prior to becoming an optically luminous quasar.

Alternatively, Villar Martín et al. (2020) suggest that the unusual spectral properties in core ERQs can be explained by their high bolometric luminosities and an intermediate orientation that results in the continuum emitting region and inner BLR being predominantly obscured whereas the outskirts of the BLR are visible. Hence, they suggest that the observed suppression in the UV and continuum along with the FWHMs of the broad lines (intermediate between Type 1 and 2 as found by Hamann et al. 2017) are explainable as an orientation effect. However, this scenario has difficulty explaining the broad blueshifted [O III] lines that are ubiquitous in ERQs (Perrotta et al. 2019) but less common in normal luminous quasars. Notably, Perrotta et al. (2019) estimate that the kinematic power of strong ERQ outflows based on [O III] emission are 1–1.5 dex higher than those of blue quasars with comparable luminosities.

Thus, there remains some ambiguity as to whether ERQs can be explained by geometry and orientation effects or whether they represent a particular outflow-dominated phase of quasar evolution. If the latter, a key question is whether their strong outflows can regulate galactic processes in their hosts.

In what follows, we summarize the physical properties of J0048-0046 and compare them to those of core ERQs. Most importantly, we consider the implications of our results on quasar-galaxy evolutionary scenarios.

6.2. Extreme NLR Outflows of J0048-0046

J0048-0046 meets the core ERQ color selection criterion with $i - W3 = 5.2$ mag (AB); however, it is at $z = 0.94$ and therefore our optical+NIR spectrum does not cover C IV $\lambda 1549$. In ordinary Type 1 quasars, Mg II $\lambda 2800$ and C IV have broadly consistent properties (Vanden Berk et al. 2001) albeit the C IV line typically has a relative blueshift to the Mg II line of a few hundred kilometers per second (Richards et al. 2002). The Mg II line in our spectrum has a low S/N and a low EW (19 Å) relative to the criterion defined for core ERQs (EW C IV > 100 Å). However, its ionization potential is much lower than that of C IV (7.6 versus 47.9 eV, respectively), and ERQs are known to have stronger high ionization lines (Hamann et al. 2017). Nonetheless, the kinematics of the Mg II line are very similar to those of C IV in ERQs: the line is moderately broad (FWHM ~ 36 Å) but lacks the broad wings typical of Type 1 quasars. While the S/N of Mg II is low, it appears to have very similar kinematics to the lines associated with the NLR ([Ne V], [O III]). The Hα line has a high EW (123 Å); however, the fact that these lines originate in both the BLR and NLR make their kinematics more difficult to interpret. The Hβ line is marred by sky residuals.

The most striking feature of the spectrum of J0048-0046 is its strong broad [Ne V] $\lambda\lambda 3345$, 3426 emission ([Ne V] $\lambda 3426$ EW = 63 Å). Unusually strong [Ne V] emission has previously been found in some Type 2 quasars (Rose et al. 2015; Yuan et al. 2016). Rose et al. (2015) deem such objects *coronal line forest forest AGNs*. These AGN additionally show signatures of [Fe VII] $\lambda\lambda 5721$, 6087, which has an ionization potential similar to [Ne V]. The latter transition is present, albeit weakly, in the NIRSPEC spectrum of J0048-0046 and shows a blueshift similar to [Ne V]. Rose et al. (2015) suggest that these emission lines originate along the inner wall of the obscuring torus, which could support the orientation hypothesis discussed above. However, the [Ne V]-strong Type 2s previously studied have very narrow lines. The extreme broadening ($\sim 4000 \, \mathrm{km \, s^{-1}}$) and blueshifting ($\sim -4000 \, \mathrm{km \, s^{-1}}$) of the [Ne V] and [O III] lines in J0048-0046 (Figure 2), suggest a different origin for the high ionization emission, perhaps in fast wind shocks as suggested by Hwang et al. (2018).

Lower redshift ERQs ($0.3 < z < 1.5$) with visibly identifiable [Ne V] are present in 17 out of 41 AGN from the Ross et al. (2015) sample where [Ne V] falls within the wavelength coverage

of BOSS. For 14 of these 17 AGN, we are able to perform the multicomponent fitting (Perrotta et al. 2019) on [Ne V] as previously carried out in Section 3. The median w_{90} value of this subsample is 3057 km s^{-1} with a standard deviation of 1303 km s^{-1}. The median v_{98} value of this subsample is -1738 km s^{-1} with a standard deviation of 924 km s^{-1}. The [Ne V] profile in J0048-0046 is then comparable to this subsample of ERQs in terms of broadening ($w_{90} = 3469$ km s^{-1}); however, it exhibits the strongest outflow ($v_{98} = -4013$ km s^{-1}). The [O III] EW is also very large (221 Å) in J0048-0046, comparable to the values found in the core ERQ sample studied by Perrotta et al. (2019). The [O III] and [Ne V] kinematics are very well matched overall (Figure 2). Notably, the higher velocity gas has a higher [Ne V]/ [Ne III] ratio (Figure 3), suggesting a link between the outflow velocity and its distance from the ionization source. Perrotta et al. (2019) find that larger [O III] line widths correlate with redder colors, which suggests that dust may play a role in driving ERQ winds (see their Figure 6). The [O III] w_{90} and $i - W3$ color of J0048-0046 place it squarely on this correlation.

Overall, we conclude that while the C IV EW of J0048-0046 is unknown, the strength of the high ionization lines and the similar [O III] kinematics to the core ERQs studied in Perrotta et al. (2019) make it likely that J0048-0046 is a low redshift core ERQ. The observed correlation between ionization and outflow velocity adds support to the hypothesis that the unique emission line properties are linked to the energetics and geometry of the outflows.

6.3. SED of J0048-0046

The SED of J0048-0046 is in stark contrast to those of typical Type 1 QSOs and highly reddened Type 1 QSOs. The optical-NIR portion is in strong agreement with Type 2 QSOs due to its strong starlight component; however, it has a substantially larger MIR flux. Overall, the SED of J0048-0046 best matches the composite SED of core ERQs from Hamann et al. (2017), although it is slightly redder. The strong stellar contribution to the SED and lack of variability at NUV-NIR wavelengths (Section 5) indicates that J0048-0046 is either a Type 2 ERQ or a Type 1 where the reddened QSO continuum contributes minimally at these wavelengths.

In Section 2.4, we noted that J0048-0046 was included in a sample of IR-bright DOGs (Toba et al. 2017). These were selected by a color of $i - W4 > 7$ mag in the redshift range of $0.05 < z < 1.02$ with detected [O III] $\lambda 5007$ in their BOSS spectra. Of the 36 sources studied in their analysis, J0048-0046 exhibits the second-most powerful outflow in [O III] and is 4σ higher than the mean of this sample. Their utilized color selection is similar to ERQ color selections and they note that four of their 36 AGN overlap with the Ross et al. (2015) ERQs. They find that IR-bright DOGs have similar, unusually large ionized outflows in [O III]. However, the IR-bright DOGs have a median bolometric luminosity of 46.02 erg s^{-1}, roughly one percent that of the core ERQs. One possibility is that ERQs and IR-bright DOGs are part of an evolutionary sequence with DOGs representing a somewhat more obscured and less active earlier phase, with J0048-0046 near the border line between the two.

6.4. Radio Emission as a By-product of Shocks

We found from the FIRST radio flux measurement of J0048-0046 (Section 2.4) that the quasar is radio quiet. The origin of

radio-quiet emission in quasars is still not fully understood as radio emission in the radio-quiet regime is too low to be explained by powerful jets originating from the AGN as observed in some quasars. A multitude of phenomena have been shown to contribute to radio-quiet emission in quasar populations, such as radio synchrotron emission as a by-product of star formation feedback (Helou et al. 1985; Fan et al. 2016; Farrah et al. 2017) young compact jets found in the host (Fanti et al. 1990), or accelerated particles produced from shocks as a result of AGN-driven winds (Zakamska & Greene 2014; Nims et al. 2015). Multiple scenarios for radio-quiet emission in core ERQs were considered by Hwang et al. (2018) and they concluded that AGN-driven winds are the most plausible explanation for the observed radio luminosities. In considering star formation as the origin of radio-quiet emission, they indicate that an SFR of 2700 $M_\odot$ yr^{-1} (Bell 2003) would be required to produce the radio luminosities of ERQs. The resulting rest-frame U-band luminosities of 10 core ERQ hosts from Zakamska et al. (2019) suggest that ERQs are not undergoing such high SFRs. Our SFR upper limit of 72 $M_\odot$ yr^{-1} (Section 4.2) further indicates that star formation is likely not the dominant cause of radio-quiet emission in ERQs.

Hwang et al. (2018) further demonstrated that core ERQs extend the relationship between [O III] line width and radio luminosity originally shown for the $z < 0.8$ Type 2 quasar sample in Zakamska & Greene (2014), suggesting that AGN-driven winds in ERQs can reach into the surrounding host galaxies and shock the ISM. Using our calculated radio luminosity (Table 1) from the reported FIRST flux density and the measured w_{90} of [O III] (4062 km s^{-1}), we find that J0048-0046 lies in the same region as ERQs in Figure 7 of Hwang et al. (2018).

6.5. Host Galaxy of J0048-0046

To understand the quasar–host galaxy interaction in core ERQs, it is critical to measure the physical conditions in the host galaxy. However, this has proven to be difficult due to the redshift of the core ERQs and their dominant nuclear point sources. HST imaging of 10 $z = 2$–3 ERQs detected only six host galaxies well enough to measure very basic structural parameters, and the absence of deep multicolor imaging precluded any assessment of the stellar population properties (Zakamska et al. 2019).

While our stellar population fitting exercise is limited by the S/N of the spectrum, it is aided by the fact that the QSO contributes only 15%–35% of the light at rest-frame wavelengths of 2000–7000 Å. We find that the host galaxy experienced a strong starburst ~400 Myr ago, which was subsequently quenched. Assuming that ERQs represent very young AGN, the age of the starburst implies a delay in the onset of AGN activity relative to star formation. This is consistent with the scenario proposed by Wild et al. (2010) where the black hole accretion rate peaks ~250 Myr after a merger-induced starburst. They postulate that the black hole is fueled by mass lost by intermediate mass stars in the bulge, but accretion of this material is suppressed at early times by supernova feedback.

The original sample of 65 ERQs from Ross et al. (2015) includes seven quasars ($0.34 < z < 1.095$), which show signatures of ongoing/recent starburst phases, three of which are post-starbursts based on their strong Balmer breaks. Notably, these three quasars are included in the broad/blueshifted [Ne V]

comparison sample discussed in Section 6.2. Given that post-starbursts make up just $\sim$2% of the galaxy population at these redshifts (Wild et al. 2016), this fraction is quite remarkable. Similar to J0048-0046, these sources may be useful cosmic laboratories to study the relationship between powerful quasar winds and the impact they have on their hosts.

The host galaxy of J0048-0046 is luminous, with $\log(L_B/L_\odot) = 11.1$. This is slightly lower than the median ($\log(L_B/L_\odot) = 11.2$) but well within the range of the quasar-subtracted host luminosities of the 10 HST-imaged core ERQs studied in Zakamska et al. (2019). These $z \sim 2.5$ core ERQs have host galaxy luminosities of $4L_B^*$, whereas the host of J0048-0046 is roughly $5L_B^*$, using L_B^* at $z \sim 1$ from Giallongo et al. (2005). In contrast, the six Type 2 quasars studied by Zakamska et al. (2019) have host luminosities around L^*.

We estimate that the host galaxy of J0048-0046 has a stellar mass between 5.6 and $9.8 \times 10^{10}\ M_\odot$. This mass is within the range ($10^{10.4}$–$10^{11.4}\ M_\odot$) found for core ERQs by Zakamska et al. (2019). Plugging our mass into the empirical relation between black hole mass and bulge mass found for Type 1 quasars at $z = 0.2$–1 (Ishino et al. 2020), we infer a black hole mass between 2.5 and $4.8 \times 10^8\ M_\odot$. Notably, the Ishino et al. M_*–M_{BH} relationship displays a large scatter (0.35 dex) and predicts a lower black hole mass than scaling relations derived for local quiescent galaxies (Kormendy & Ho 2013). This scatter, combined with the fact that J0048-0046 has a large uncertainty for its stellar mass, an unknown bulge to disk ratio, and the fact that the Ishino et al. (2020) scaling relation is derived from measurements of quasars which are unambiguously of Type 1, means that our estimate of the black hole mass is likely on the order of a magnitude uncertain. Computing the Eddington luminosity for our inferred black hole masses yields $\log L_{Edd} = 46.5$–46.8. Comparing these values to the bolometric luminosities given in Table 1 suggests that the quasar is radiating near its Eddington luminosity with $L_{bol}/L_{edd} \sim 1.23$, consistent with an average $L_{bol}/L_{edd} = 1.03$ in the Perrotta et al. (2019) core ERQs.

Another interesting result found by Zakamska et al. (2019) was that only 20%–30% of their HST-imaged ERQs showed merger signatures, in contrast to the high fraction expected at $z = 2$–3. They suggest that the near-Eddington accretion and strong feedback of ERQs are associated with relatively late stages of mergers, which have early-type remnants. However, they note that merger signatures could be hidden at optical wavelengths or that gas instabilities within ERQ disks could be an alternate triggering mechanism. The apparent tidal bridge feature between J0048-0046 and its companion (Figure 5) indicates that a merger event may have been the contributing factor to its star formation history and its eventual high AGN accretion rate. The overall picture for ERQs will become more clear as we build up larger samples of ERQs with high resolution imaging.

A key result of our SSP analysis was our finding of low dust attenuation in the host galaxy of J0048-0046 ($A_V = 0.17$). This indicates that the heavy extinction/reddening in core ERQs may be representative solely of dust obscuration around the AGN and it disfavors the proposed evolutionary scenario (Glikman et al. 2007; Urrutia et al. 2009; Banerji et al. 2012; Glikman et al. 2012; Assef et al. 2013; Glikman et al. 2013) where the ERQs are transitioning between a dusty submilli-meter galaxy and a luminous QSO. The post-starburst nature of

the host galaxy likewise contradicts this simple evolutionary paradigm.

An interesting question is whether the QSO may be helping to maintain the galaxy in its post-starburst state. Using our [O III] luminosity and v_{98} value, we follow the exact procedure laid out in Section 5.1 of Perrotta et al. (2019) to estimate the outflow's kinetic power in J0048-0046. We obtain $\log(\dot{E}_k) = 45.4\ \mathrm{erg\ s}^{-1}$, within the range of the Perrotta et al. (2019) core ERQ sample and shifted above other quasar samples (see Perrotta et al. 2019, Figure 9). This yields $\dot{E}_k/L_{bol} = 6\%$–9% depending on the adopted bolometric luminosity from Table 1. Various simulations have suggested that values at or above 5% of the total radiated energy are required for the outflow to have a significant impact on the host and quench/regulate its star formation (Scannapieco & Oh 2004; Di Matteo et al. 2005; Hopkins et al. 2005, 2008). Hence, the powerful outflow J0048-0046 exhibits has the potential to greatly disrupt the ISM of the host and may have a connection to its post-starburst state. In order to further consider the relationship between galactic-scale properties and quasar energetics, future stellar population analysis of ERQs host galaxies, including the subsample from Ross et al. (2015) mentioned above, are necessary to consider their host's evolutionary state in relation to their AGN-powered winds.

7. Summary and Conclusions

Apparent peculiarities in the optical spectrum and the NUV to FIR SED of the $z = 0.94$ quasar, J0048-0046, present it as a distinct source in the context of typical Type 1 and 2 quasars. With a more detailed analysis (Section 3), we find that it is most likely an ERQ (Ross et al. 2015; Hamann et al. 2017), a candidate young quasar that has just recently begun AGN activity and is in the process of blowing out gas at extreme velocities. While properties of these recently discovered ERQs have been studied and discussed extensively (Perrotta et al. 2019; Zakamska et al. 2019), J0048-0046 has the key advantage of having a spectroscopically resolvable host galaxy to constrain its star formation history in addition to high-cadence, multi-epoch photometry to investigate for variability. Both of these features make J0048-0046 unique in the context of ERQs and can offer insight into the nature of young AGN and their properties.

J0048-0046 is a luminous AGN ($L_{bol} = 10^{46.5}\ \mathrm{erg\ s}^{-1}$) that exhibits powerful outflows in the NLR [O III] λ5007 and [Ne V] λ3426 with velocity widths (w90) around 4000 km $^{-1}$ (see Figure 2, Section 3). The [O III] velocity width is in-line with those displayed in core ERQs (Perrotta et al. 2019). It shows unusually high line ratios of [Ne V] λ3426/[Ne III] λ3869 and [O III] λ5007/[O II] λ3728 compared to typical quasars. Comparing the line profiles of [Ne V] and [Ne III], we find that higher ionization occurs at larger outflow speeds which indicates a connection between the outflow and the ionizing process. Additionally, its radio-quiet emission could possibly arise from wind shocks driven by the powerful outflow (Section 6.4). The connection between high ionization lines with high velocities supports the idea that the peculiar emission line properties in ERQs are linked to outflows rather than orientation.

J0048-0046 meets the optical to MIR color selection criterion of $i - W3 > 4.6$ imposed to select ERQs in Hamann et al. (2017). An analysis of the source's SED (Figure 4, Section 3.2) clearly shows that it is different than both standard

and heavily reddened Type 1 quasars. Its dominance by starlight in the optical to NIR gives it a similar shape to Type 2 quasars at these wavelengths, but its SED deviates strongly in the MIR. We find that J0048-0046 is most similar to the median SED of the *core* ERQs from Hamann et al. (2017), albeit slightly redder.

In Section 4.2, we take advantage of the strong host galaxy continuum apparent in J0048-0046 (Figure 7) to characterize the stellar population of an ERQ for the first time. We find that the massive host galaxy ($\log(M/M_\odot) = 10.7$–11) underwent a strong starburst 400 Myr ago before it was abruptly quenched. If ERQs are indeed young AGN, then this timescale could indicate a connected offset between the starburst and the beginning of AGN activity as suggested by Wild et al. (2010). The low extinction in the host is in contrast to expectations from galactic evolutionary models and may suggest that ERQs are not dusty submillimeter galaxies in transition.

Based on J0048-0046 and the neighboring galaxy's morphology, it is possible that the post-starburst phase of J0048-0046 has arisen from a major merger. Given the rareness of post-starbursts ($\sim 2\%$ of all massive galaxies at $z \sim 1$; Wild et al. 2016) and ERQs ($<1\%$ of luminous AGN; Hamann et al. 2017), it seems unlikely that J0048-0046 is a member of both populations by coincidence. Instead, our estimated time lag between peak starburst and AGN states (again, in-line with Wild et al. 2010) makes an evolutionary connection between ERQs and post-starbursts seem more likely. Future SSP analysis of larger ERQ samples with resolvable host galaxies are necessary to solidify these findings.

The multi-epoch SDSS data release and S82 catalog photometry initially present J0048-0046 as a variable AGN. However, careful photometric analysis using GALFITM indicates that successful deblending of J0048+0046 and its companion are not always produced by the SDSS pipeline. We find that J0048-0046 is not variable at rest frame 0.24–2.4 μm wavelengths. Combined with the dominance of host galaxy light in the optical spectrum, this may point to J0048-0046 being a Type 2 ERQ or a Type 1 where the contribution of the AGN continuum to the total light at these wavelengths is minimal.

We conclude that J0048-0046 is a $z \sim 1$ core ERQ and poses a unique opportunity to study the stellar populations the first time in such an object. The strongly broad and blueshifted [Ne V] is an indicator that the AGN is driving strong, high ionization outflows. In future work, we will attempt to spatially resolve this outflow and constrain the extent to which it reaches into the host galaxy of J0048-0046 (Tremonti et al. 2020).

ORCID iDs

Cameren Swiggum https://orcid.org/0000-0001-9201-5995
Christy Tremonti https://orcid.org/0000-0003-3097-5178
Serena Perrotta https://orcid.org/0000-0002-2451-9160
Ryan C. Hickox https://orcid.org/0000-0003-1468-9526
Alison L. Coil https://orcid.org/0000-0002-2583-5894
Paul H. Sell https://orcid.org/0000-0003-1771-5531
Gregory Mosby https://orcid.org/0000-0002-5982-566X

References

Abazajian, K. N., Adelman-McCarthy, J. K., Agüeros, M. A., et al. 2009, ApJS, 182, 543
Abel, N. P., & Satyapal, S. 2008, ApJ, 678, 686
Alatalo, K., Cales, S. L., Rich, J. A., et al. 2016, ApJS, 224, 38
Alexandroff, R. M., Zakamska, N. L., Barth, A. J., et al. 2018, MNRAS, 479, 4936
Anderson, J., & King, I. R. 2000, PASP, 112, 1360
Assef, R. J., Stern, D., Kochanek, C. S., et al. 2013, ApJ, 772, 26
Astropy Collaboration, Robitaille, T. P., Tollerud, E. J., et al. 2013, A&A, 558, A33
Banerji, M., McMahon, R. G., Hewett, P. C., et al. 2012, MNRAS, 427, 2275
Barth, A. J., Voevodkin, A., Carson, D. J., et al. 2014, AJ, 147, 12
Becker, R. H., White, R. L., & Helfand, D. J. 1995, ApJ, 450, 559
Bell, E. F. 2003, ApJ, 586, 794
Bershady, M. A., Trevese, D., & Kron, R. G. 1998, ApJ, 496, 103
Bieri, R., Dubois, Y., Rosdahl, J., et al. 2017, MNRAS, 464, 1854
Blandford, R. D., & Begelman, M. C. 2004, MNRAS, 349, 68
Blecha, L., Snyder, G. F., Satyapal, S., et al. 2018, MNRAS, 478, 3056
Bradley, L., Sipőcz, B., Robitaille, T., et al. 2021, astropy/photutils: 1.3.0, v1.3.0, Zenodo, doi:10.5281/zenodo.5796924
Bundy, K., Leauthaud, A., Saito, S., et al. 2015, ApJS, 221, 15
Calzetti, D., Armus, L., Bohlin, R. C., et al. 2000, ApJ, 533, 682
Cappellari, M. 2017, MNRAS, 466, 798
Carniani, S., Marconi, A., Maiolino, R., et al. 2015, A&A, 580, A102
Carniani, S., Marconi, A., Maiolino, R., et al. 2016, A&A, 591, A28
Casali, M., Adamson, A., Alves de Oliveira, C., et al. 2007, A&A, 467, 777
Chambers, K. C., Magnier, E. A., Metcalfe, N., et al. 2016, arXiv:1612.05560
Conroy, C., & Gunn, J. E. 2010, ApJ, 712, 833
Conroy, C., Gunn, J. E., & White, M. 2009, ApJ, 699, 486
Crawford, S. M., Still, M., Schellart, P., et al. 2010, Proc. SPIE, 7737, 773725
Dawson, K. S., Schlegel, D. J., Ahn, C. P., et al. 2013, AJ, 145, 10
Dey, A., Schlegel, D. J., Lang, D., et al. 2019, AJ, 157, 168
Di Matteo, T., Springel, V., & Hernquist, L. 2005, Natur, 433, 604
DiPompeo, M. A., Hickox, R. C., Carroll, C. M., et al. 2018, ApJ, 856, 76
Dudzevičiūtė, U., Smail, I., Swinbank, A. M., et al. 2020, MNRAS, 494, 3828
Duras, F., Bongiorno, A., Ricci, F., et al. 2020, A&A, 636, A73
Eisenstein, D. J., Weinberg, D. H., Agol, E., et al. 2011, AJ, 142, 72

Fabian, A. C. 2012, ARA&A, 50, 455
Fan, L., Han, Y., Nikutta, R., et al. 2016, ApJ, 823, 107
Fanti, R., Fanti, C., Schilizzi, R. T., et al. 1990, A&A, 231, 333
Farrah, D., Petty, S., Connolly, B., et al. 2017, ApJ, 844, 106
Flaugher, B., Diehl, H. T., Honscheid, K., et al. 2015, AJ, 150, 150
Fliri, J., & Trujillo, I. 2016, MNRAS, 456, 1359
Gaskell, C. M., & Benker, A. J. 2007, arXiv:0711.1013
Giallongo, E., Salimbeni, S., Menci, N., et al. 2005, ApJ, 622, 116
Gilli, R., Vignali, C., Mignoli, M., et al. 2010, A&A, 519, A92
Glikman, E., Helfand, D. J., White, R. L., et al. 2007, ApJ, 667, 673
Glikman, E., Urrutia, T., Lacy, M., et al. 2012, ApJ, 757, 51
Glikman, E., Urrutia, T., Lacy, M., et al. 2013, ApJ, 778, 127
Gunn, J. E., Siegmund, W. A., Mannery, E. J., et al. 2006, AJ, 131, 2332
Hamann, F., Zakamska, N. L., Ross, N., et al. 2017, MNRAS, 464, 3431
Harrison, C. M., Alexander, D. M., Mullaney, J. R., et al. 2014, MNRAS, 441, 3306
Helou, G., Soifer, B. T., & Rowan-Robinson, M. 1985, ApJL, 298, L7
Hickox, R. C., Myers, A. D., Greene, J. E., et al. 2017, ApJ, 849, 53
Hopkins, P. F., Cox, T. J., Dutta, S. N., et al. 2009, ApJS, 181, 135
Hopkins, P. F., Hernquist, L., Cox, T. J., et al. 2005, ApJ, 630, 705
Hopkins, P. F., Hernquist, L., Cox, T. J., et al. 2006, ApJS, 163, 1
Hopkins, P. F., Hernquist, L., Cox, T. J., et al. 2008, ApJS, 175, 356
Hopkins, P. F., Hernquist, L., Cox, T. J., et al. 2008, ApJ, 679, 156
Hopkins, P. F., Torrey, P., Faucher-Giguère, C.-A., et al. 2016, MNRAS, 458, 816
Hwang, H.-C., Zakamska, N. L., Alexandroff, R. M., et al. 2018, MNRAS, 477, 830
Ishibashi, W., & Fabian, A. C. 2015, MNRAS, 451, 93
Ishibashi, W., & Fabian, A. C. 2016, MNRAS, 457, 2864
Ishino, T., Matsuoka, Y., Koyama, S., et al. 2020, PASJ, 72, 83
Johnson, B. D., Leja, J., Conroy, C., et al. 2021, ApJS, 254, 22
Kim, S., Prato, L., & McLean, I. 2015, REDSPEC: NIRSPEC Data Reduction, Astrophysics Source Code Library, ascl:1507017
Kobulnicky, H. A., Nordsieck, K. H., Burgh, E. B., et al. 2003, Proc. SPIE, 4841, 1634
Kormendy, J., & Ho, L. C. 2013, ARA&A, 51, 511
Krumholz, M. R., & Thompson, T. A. 2012, ApJ, 760, 155
Krumholz, M. R., & Thompson, T. A. 2013, MNRAS, 434, 2329
Lang, D. 2014, AJ, 147, 108
Lang, D., Hogg, D. W., & Schlegel, D. J. 2016, AJ, 151, 36
Lawrence, A., Warren, S. J., Almaini, O., et al. 2007, MNRAS, 379, 1599
Leja, J., Carnall, A. C., Johnson, B. D., et al. 2019, ApJ, 876, 3
Liu, G., Zakamska, N. L., Greene, J. E., et al. 2013, MNRAS, 436, 2576
Lupton, R., Gunn, J. E., Ivezić, Z., et al. 2001, in ASP Conf. Ser. 238, Astronomical Data Analysis Software and Systems X, ed. F. R. Jr. Harnden et al. (San Francisco, CA: ASP), 269
Mainzer, A., Bauer, J., Grav, T., et al. 2011, ApJ, 731, 53
Markwardt, C. B. 2009, in ASP Conf. Ser. 411, Astronomical Data Analysis Software and Systems XVIII, ed. D. A. Bohlender (San Francisco, CA: ASP), 251
Martin, D. C., Fanson, J., Schiminovich, D., et al. 2005, ApJL, 619, L1
McLean, I. S., Becklin, E. E., & Bendiksen, O. 1998, Proc. SPIE, 3354, 566
Mihos, J. C., & Hernquist, L. 1994, ApJL, 431, L9
Moustakas, J., Kennicutt, R. C., & Tremonti, C. A. 2006, ApJ, 642, 775
Mullaney, J. R., Alexander, D. M., Fine, S., et al. 2013, MNRAS, 433, 622
Murray, N., Quataert, E., & Thompson, T. A. 2005, ApJ, 618, 569
Nims, J., Quataert, E., & Faucher-Giguère, C.-A. 2015, MNRAS, 447, 3612
Peng, C. Y., Ho, L. C., Impey, C. D., et al. 2002, AJ, 124, 266
Planck Collaboration, Aghanim, N., Akrami, Y., et al. 2020, A&A, 641, A6
Pennell, A., Runnoe, J. C., & Brotherton, M. S. 2017, MNRAS, 468, 1433
Perrotta, S., Hamann, F., Zakamska, N. L., et al. 2019, MNRAS, 488, 4126
Polletta, M., Weedman, D., Hönig, S., et al. 2008, ApJ, 675, 960
Proga, D., & Kallman, T. R. 2004, ApJ, 616, 688
Richards, G. T., Vanden Berk, D. E., Reichard, T. A., et al. 2002, AJ, 124, 1
Rose, M., Elvis, M., Crenshaw, M., et al. 2015, MNRAS, 451, L11
Ross, N. P., Hamann, F., Zakamska, N. L., et al. 2015, MNRAS, 453, 3932
Runnoe, J. C., Brotherton, M. S., & Shang, Z. 2012, MNRAS, 426, 2677
Rupke, D. S. N., & Veilleux, S. 2011, ApJL, 729, L27
Rupke, D. S. N., & Veilleux, S. 2013, ApJ, 768, 75
Salim, S., Boquien, M., & Lee, J. C. 2018, ApJ, 859, 11
Salpeter, E. E. 1955, ApJ, 121, 161
Sanders, D. B., Soifer, B. T., Elias, J. H., et al. 1988, ApJ, 325, 74
Sarajedini, V. L., Koo, D. C., Phillips, A. C., et al. 2006, ApJS, 166, 69
Scannapieco, E., & Oh, S. P. 2004, ApJ, 608, 62
Science Software Branch at STScI 2012, pyraf-dbsp: Reduction pipeline for the Palomar Double Beam Spectrograph, Astrophysics Source Code Library, ascl:1207.011
Sell, P. H., Tremonti, C. A., Hickox, R. C., et al. 2014, MNRAS, 441, 3417
Shen, X., Hopkins, P. F., Faucher-Giguère, C.-A., et al. 2020, MNRAS, 495, 3252
Shen, Y. 2016, ApJ, 817, 55
Shen, Y., Richards, G. T., Strauss, M. A., et al. 2011, ApJS, 194, 45
Simpson, J. M., Swinbank, A. M., Smail, I., et al. 2014, ApJ, 788, 125
Smee, S. A., Gunn, J. E., Uomoto, A., et al. 2013, AJ, 146, 32
Stoughton, C., Lupton, R. H., Bernardi, M., et al. 2002, AJ, 123, 485
Thompson, T. A., Fabian, A. C., Quataert, E., et al. 2015, MNRAS, 449, 147
Toba, Y., Bae, H.-J., Nagao, T., et al. 2017, ApJ, 850, 140
Tremonti, C. A., Coil, A. L., Diamond-Stanic, A. M., et al. 2020, HST Proposal ID 16291
Urrutia, T., Becker, R. H., White, R. L., et al. 2009, ApJ, 698, 1095
Urrutia, T., Lacy, M., & Becker, R. H. 2008, ApJ, 674, 80
Vanden Berk, D. E., Richards, G. T., Bauer, A., et al. 2001, AJ, 122, 549
Vaughan, S., Edelson, R., Warwick, R. S., et al. 2003, MNRAS, 345, 1271
Veilleux, S., Rupke, D. S. N., Kim, D.-C., et al. 2009, ApJS, 182, 628
Vernaleo, J. C., & Reynolds, C. S. 2006, ApJ, 645, 83
Vika, M., Bamford, S. P., Häußler, B., et al. 2013, MNRAS, 435, 623
Villar Martín, M., Perna, M., Humphrey, A., et al. 2020, A&A, 634, A116
Wild, V., Almaini, O., Dunlop, J., et al. 2016, MNRAS, 463, 832
Wild, V., Heckman, T., & Charlot, S. 2010, MNRAS, 405, 933
Wild, V., Walcher, C. J., Johansson, P. H., et al. 2009, MNRAS, 395, 144
Wright, E. L., Eisenhardt, P. R. M., Mainzer, A. K., et al. 2010, AJ, 140, 1868
Xu, C., Livio, M., & Baum, S. 1999, AJ, 118, 1169
Yan, R., Newman, J. A., Faber, S. M., et al. 2006, ApJ, 648, 281
Yip, C. W., Connolly, A. J., Vanden Berk, D. E., et al. 2009, AJ, 137, 5120
Yuan, S., Strauss, M. A., & Zakamska, N. L. 2016, MNRAS, 462, 1603
Zahid, H. J., Geller, M. J., Fabricant, D. G., et al. 2016, ApJ, 832, 203
Zakamska, N. L., & Greene, J. E. 2014, MNRAS, 442, 784
Zakamska, N. L., Strauss, M. A., Krolik, J. H., et al. 2003, AJ, 126, 2125
Zakamska, N. L., Sun, A.-L., Strauss, M. A., et al. 2019, MNRAS, 489, 497